Article

SOURCE DATA | TRANSPARENT PROCESS | OPEN ACCESS

THE EMBO JOURNAL

Replication-induced DNA secondary structures drive fork uncoupling and breakage

Sophie L Williams[1], Corella S Casas-Delucchi[1], Federica Raguseo[2,3], Dilek Guneri[4], Yunxuan Li[5], Masashi Minamino[6], Emma E Fletcher[7], Joseph TP Yeeles[7], Ulrich F Keyser[5], Zoë AE Waller[4], Marco Di Antonio[2,3,6] & Gideon Coster[1,*]

Abstract

Sequences that form DNA secondary structures, such as G-quadruplexes (G4s) and intercalated-Motifs (iMs), are abundant in the human genome and play various physiological roles. However, they can also interfere with replication and threaten genome stability. Multiple lines of evidence suggest G4s inhibit replication, but the underlying mechanism remains unclear. Moreover, evidence of how iMs affect the replisome is lacking. Here, we reconstitute replication of physiologically derived structure-forming sequences to find that a single G4 or iM arrest DNA replication. Direct single-molecule structure detection within solid-state nanopores reveals structures form as a consequence of replication. Combined genetic and biophysical characterisation establishes that structure stability and probability of structure formation are key determinants of replisome arrest. Mechanistically, replication arrest is caused by impaired synthesis, resulting in helicase-polymerase uncoupling. Significantly, iMs also induce breakage of nascent DNA. Finally, stalled forks are only rescued by a specialised helicase, Pif1, but not Rrm3, Sgs1, Chl1 or Hrq1. Altogether, we provide a mechanism for quadruplex structure formation and resolution during replication and highlight G4s and iMs as endogenous sources of replication stress.

Keywords DNA replication; DNA secondary structures; genome stability; G-quadruplex and i-Motif; replication stress

Subject Category DNA Replication, Recombination & Repair

DOI 10.15252/embj.2023114334 | Received 20 April 2023 | Revised 20 September 2023 | Accepted 21 September 2023

The EMBO Journal (2023) e114334

Introduction

Eukaryotic DNA replication is a highly regulated process carried out by a complex molecular machine known as the replisome (Bell & Labib, 2016). Parental duplex DNA is unwound by the replicative helicase, CMG, and nascent DNA is subsequently synthesised by polymerase ε on the leading strand, or polymerase δ on the lagging strand. The replisome must replicate all regions of the genome accurately while encountering various obstacles such as DNA damage, protein barriers and transcription-replication collisions (reviewed in Zeman & Cimprich, 2014). All of these can lead to replication stress, which poses a challenge to genome integrity (Gaillard *et al*, 2015).

Another potential barrier to replisome progression is the DNA template itself. Aside from the canonical B-DNA conformation, certain DNA sequences can fold into secondary structures, particularly from ssDNA exposed during replication. Examples of well-characterised secondary structures include hairpin (Gacy *et al*, 1995; Nadel *et al*, 1995), triplex (H-DNA) (Mirkin *et al*, 1987), G-quadruplex (G4) (Fry & Loeb, 1994) and intercalated-Motif (iM) (Gehring *et al*, 1993) structures, which are thought to act as barriers to replication. For example, hairpin-forming repeats cause replication stalling in bacteria, yeast, and human cells (Voineagu *et al*, 2008). Moreover, two unbiased studies have mapped sites of replication fork collapse *in vivo*, highlighting poly(dA) sites (Tubbs *et al*, 2018) and a variety of structure-forming repeats (Shastri *et al*, 2018). Therefore, secondary structures may be responsible for the fact that repetitive sequences are unstable and give rise to genomic instability (reviewed in Brown & Freudenreich, 2021).

G4 structures are formed from guanine-rich sequences through the stacking of G quartets formed by Hoogsteen base pairing (Sen & Gilbert, 1988). Their abundance increases during S-phase, suggesting they arise as a consequence of replication (Biffi *et al*, 2013; Di Antonio *et al*, 2020). G4-forming sequences are defined by a motif consisting of four consecutive tracts of at least three guanines (G-tracts), separated by one to seven non-G nucleotides ($G_3N_{1\text{-}7}G_3N_{1\text{-}7}G_3N_{1\text{-}7}G_3$) (Huppert & Balasubramanian, 2005) which are referred to as 'loops'. The length and composition of these loops affects the stability of the G4 structure. For example, shorter loops composed of thymine residues correlate with more thermally

1 Genome Replication Lab, Division of Cancer Biology, Institute of Cancer Research, Chester Beatty Laboratories, London, UK
2 Chemistry Department, Imperial College London, MSRH, London, UK
3 Institute of Chemical Biology, MSRH, London, UK
4 UCL, School of Pharmacy, London, UK
5 Cavendish Laboratory, University of Cambridge, Cambridge, UK
6 Francis Crick Institute, London, UK
7 MRC Laboratory of Molecular Biology, Cambridge, UK
*Corresponding author. Tel: +442034377582; E-mail: gideon.coster@icr.ac.uk

stable structures, while longer loops result in less stable structures (Piazza *et al*, 2015). G4s can exist in a variety of structural topologies, depending on the orientation of the G-rich strands relative to one another (parallel, anti-parallel or hybrid; Ou *et al*, 2008). G4-forming sequences are abundant in the human genome and are known to have a range of physiological roles. Firstly, they have been associated with telomere maintenance (Maiti, 2010). Secondly, they are enriched in promoter regions (Chambers *et al*, 2015) where they can affect the transcriptional state of genes (reviewed in Robinson *et al*, 2021). More recently, ChIP-Seq of G4-structures on a genome-wide scale revealed that these structures mark sites of actively transcribed genes (Hansel-Hertsch *et al*, 2016). Finally, they are implicated in human diseases. For example, G4s correlate with telomere fragility and induce both genetic and epigenetic instability (Vannier *et al*, 2013; Schiavone *et al*, 2014; Papadopoulou *et al*, 2015) and have been shown to disrupt repressive chromatin structures (Sarkies *et al*, 2010). Moreover, G4s, such as those found at the *c-myc* gene promoter, are enriched at mutation hotspots in an array of cancers (De & Michor, 2011; Wang & Vasquez, 2017).

i-Motifs arise from cytosine-rich DNA and therefore, in genomic contexts, can often be found on the opposite strand to G4s, for example at telomeres (Zeraati *et al*, 2018). These structures are held together by hemi-protonated cytosine-cytosine base pairs ($C:C^+$) and are stabilised by low pH (Gehring *et al*, 1993). Although the existence of iMs has long been established, there has been speculation about their biological relevance due to their apparent requirement for acidic conditions. However, recent studies have shown that certain iMs can form at neutral pH (Wright *et al*, 2017), requiring longer tracts of cytosines with a proposed consensus of four consecutive tracts of at least five cytosines, separated by 1–19 non-C nucleotides ($C_5N_{1-19}C_5N_{1-19}C_5N_{1-19}C_5$) (Wright *et al*, 2017). The thermal stability of iMs can be determined similarly to G4s by measuring the melting temperature of the structure. In addition to temperature, iM stability can be affected by the local pH, often described by the transitional pH (pH_T) – the pH at which the sequence is 50% folded (Wright *et al*, 2017). Similar to G4s, a longer tract of Cs and a shorter loop length creates a more stable iM. In contrast to G4s, iMs can only adopt an anti-parallel conformation. Although not highly prevalent in the yeast genome, a previous study has described a sequence on chromosome IV of *S. cerevisiae* that can fold into an iM structure (Kshirsagar *et al*, 2017). In addition to this, iMs can be found at transcription start sites and in the promoters of oncogenes, such as *BCL2* (Kendrick *et al*, 2014), *HRAS* (Miglietta *et al*, 2015), *KRAS* (Kaiser *et al*, 2017), *c-MYC* (Simonsson *et al*, 2000) and *VEGF* (Guo *et al*, 2008).

Many studies have indicated that G4s can impact replication *in vivo*. In the absence of specialised helicases, such as Pif1, G4s positioned on the leading strand template can undergo rearrangements and mutations (Lopes *et al*, 2011). While the replication machinery stalls at G4-forming sequences in a variety of organisms, there is conflicting evidence of stalling on the leading versus lagging strand template (Sarkies *et al*, 2010; Lopes *et al*, 2011; Paeschke *et al*, 2011; Dahan *et al*, 2018). In addition, a recent super-resolution microscopy study demonstrated that replication associated G4s interfere with replication stress signalling (Lee *et al*, 2021). Despite the abundance of evidence that G4s can interfere with replication, the underlying trigger remains unknown. Moreover, the mechanism of stalling and which replisome components are affected remain unclear.

Primer extension assays have demonstrated that structure-forming sequences inhibit synthesis. A variety of G4-forming sequences are sufficient to inhibit a range of polymerases *in vitro*, including the replicative polymerases ε and δ (Lormand *et al*, 2013; Edwards *et al*, 2014; Sparks *et al*, 2019b; Murat *et al*, 2020). There is some evidence that polymerase inhibition is affected not only by the stability of the G4 but also its topology (Takahashi *et al*, 2017). DNA synthesis through G4s can be aided by accessory factors such as specialised G4-unwinding helicases, including Pif1, REV1 and FANCJ (Salas *et al*, 2006; Fan *et al*, 2009; Ray *et al*, 2013; Sparks *et al*, 2019b). However, these studies were carried out with pre-folded G4 structures using isolated polymerases. Whether such structures can form in the context of dsDNA unwound by CMG and how G4s affect the complete eukaryotic replisome is unknown.

Much less is known about the effect of iM structures on eukaryotic DNA replication. The only available data are from primer extension assays, which have demonstrated that iMs can inhibit DNA synthesis by viral or prokaryotic polymerases *in vitro* (Catasti *et al*, 1997; Takahashi *et al*, 2017; Murat *et al*, 2020).

Recent work from our laboratory demonstrated that a variety of repetitive sequences stall the eukaryotic replisome. These include tracts of $poly(dG)_n$ and $poly(dC)_n$ sequences, which can form G4s or iMs, respectively (Casas-Delucchi *et al*, 2022). These results are supported by recent work from the Remus lab, which demonstrated that $poly(dG)_n$ tracts stall the eukaryotic replisome when initially stabilised by an R-loop. This study also highlighted the ability of a pre-formed G4 (generated from the sequence $(GGGT)_4$) to inhibit unwinding by the CMG helicase (Kumar *et al*, 2021). $Poly(dG)_n$ and $poly(dC)_n$ sequences are unique types of G4 and iM-forming sequences due to their homopolymeric nature, and the stability and type of structures they form is highly polymorphic and thus difficult to study. As such, these sequences may not be representative of physiological G4 and iM-forming sequences. Yeast telomeric DNA alone does not affect replisome progression *in vitro*, and replication stalling is only seen when the telomeric binding protein Rap1 is present (Douglas & Diffley, 2021). However, yeast telomeres are relatively weak G4-forming sequences. Whether G4 and iM-forming sequences found in the human genome are sufficient to stall replication remains unclear.

Here, we carry out an extensive study on physiologically derived G4 and iM sequences and investigate how they impact eukaryotic replication. Using a reconstituted budding yeast DNA replication system, we find that a single G4 or iM-forming sequence is sufficient to cause replisome stalling. The ability of these sequences to stall replication correlated with their ability to form stable structures, strongly suggesting that secondary structure formation was the underlying trigger for replication stalling. Interestingly, CMG was able to unwind past these sequences, while DNA synthesis by polymerase ε was inhibited, leading to helicase-polymerase uncoupling and exposure of ssDNA. Direct detection of secondary structures by single-molecule sensing using solid-state nanopores established the lack of pre-formed structures prior to replication, whereas conditions that enhanced replication fork uncoupling led to increased fork stalling. Together, these observations support a model whereby replication-dependent structures arise behind CMG on ssDNA exposed during unwinding, resulting in inhibition of polymerase activity. Remarkably, stalling could only be rescued by the G4-unwinding helicase Pif1, but not by other implicated helicases – Rrm3, Sgs1, Chl1 or

Table 1. Sequences of G4 oligonucleotides and their biophysical properties.

Substrate	Sequence (5′ -> 3′)	Buffer	UV Melting T_M (°C)	G4 forming?
c-MYC PU22	TGAGGGTGGGTAGGGTGGGTAA	KCl	89.3	Yes
c-MYC PU22	TGAGGGTGGGTAGGGTGGGTAA	LiCl	40.6	Yes
c-MYC PU22 MUT	TGAG**A**GTG**A**GTAG**A**GTG**A**GTAA	KCl	43.2	No
c-MYC PU22 MUT	TGAG**A**GTG**A**GTAG**A**GTG**A**GTAA	LiCl	51.2	No
(GGGT)4	GGGTGGGTGGGTGGGT	KCl	91.4	Yes
(GGGT)4	GGGTGGGTGGGTGGGT	LiCl	68.3	Yes
(GGGT)3	GGGTGGGTGGGT	KCl	61.5	Yes
(GGGT)3	GGGTGGGTGGGT	LiCl	40.8	Not by TDS
CEB25L111(T)	AAGGGTGGGTGGGTGGGTGTGAGTGTGGGTGTGGAGGTAGATGT	KCl	91	Yes
CEB25L111(T)	AAGGGTGGGTGGGTGGGTGTGAGTGTGGGTGTGGAGGTAGATGT	LiCl	58	Yes
CEB25L111(A)	AAGGG**A**GGG**A**GGG**A**GGGTGTGAGTGTGGGTGTGGAGGTAGATGT	KCl	83.6	Yes
CEB25L111(A)	AAGGG**A**GGG**A**GGG**A**GGGTGTGAGTGTGGGTGTGGAGGTAGATGT	LiCl	n/a	Not by TDS
(TTAGGG)4	TTAGGGTTAGGGTTAGGGTTAGGG	KCl	66.2	Yes
(TTAGGG)4	TTAGGGTTAGGGTTAGGGTTAGGG	LiCl	41	Yes
Bu1A G4	GGGCTGGGTGGGTGCTGTCAAGGGCTGGG	KCl	82.5	Yes
Bu1A G4	GGGCTGGGTGGGTGCTGTCAAGGGCTGGG	LiCl	39.7	Yes
(GGGGCC)6	GGGGCCGGGGCCGGGGCCGGGGCCGGGGCCGGGGCC	KCl	n/a	n/a
(GGGGCC)6	GGGGCCGGGGCCGGGGCCGGGGCCGGGGCCGGGGCC	LiCl	n/a	n/a
Poly(dG)16	GGGGGGGGGGGGGGGG	KCl	n/a	n/a
Poly(dG)16	GGGGGGGGGGGGGGGG	LiCl	n/a	n/a

Hrq1, highlighting the specificity of this enzyme. Moreover, we found that iMs can cause DNA breakage.

Altogether, this study describes the response of the eukaryotic replisome to a variety of physiological structure-forming motifs and highlights their ability to induce replication stress. This may provide a potential mechanism as to why these sequences are both genetically and epigenetically unstable and may explain their high mutational frequencies in cancer.

Results

The replisome stalls at a single quadruplex-forming sequence

To establish how quadruplex-forming sequences affect the eukaryotic replisome, we cloned several well-characterised G4- and iM-forming sequences into a 9.8 kb plasmid. These were used to generate substrates for *in vitro* eukaryotic replication using purified budding yeast proteins (Yeeles *et al*, 2015, 2017). The G4-forming sequences tested include one of the most well-characterised G4s found in the human genome, *c-MYC* Pu22. This is a 22-nt-long segment derived from the human *c-MYC* promoter region (Dai *et al*, 2011) which is frequently mutated in cancers. Other G4-forming sequences tested include (i) the human telomeric repeat sequence $(TTAGGG)_4$, (ii) the Bu1 + 3.5 G4 motif (derived from the avian DT40 genome) which induces replication-dependent epigenetic silencing (Schiavone *et al*, 2014), (iii) the CEB25 L111(T) motif derived from the naturally occurring human CEB25 mini-satellite, where all three loops have been modified to a single thymine, leading to a thermally stable G4 structure (Piazza *et al*, 2015), (iv) the GGGGCC repeat of the C9orf72 gene which is associated with familial amyotrophic lateral sclerosis (Thys & Wang, 2015), (v) a repetitive sequence that forms a strong G4 and occurs roughly 1,000 times in the human genome $(GGGT)_4$, and (vi) a tract of $poly(dG)_{16}$ which has previously been shown to induce replication stalling (Casas-Delucchi *et al*, 2022) (Table 1). Selection of iM sequences was based on their ability to form secondary structures at physiological pH (Wright *et al*, 2017). These exist in the human genome and are derived from the promoter regions of (i) DAP, (ii) DUX4L22, (iii) SNORD112, (iv) AC017019.1, (v) PIM1 and (vi) ZBTB7B (Table 2). Sequences were cloned 3 kb downstream of the ARS306 origin, from which site-specific replisome loading and firing occurs (Fig 1A). As replication initiates from a defined site in the template, we can infer the identity of the leading and lagging nascent strands. The structure-forming sequences we refer to throughout the manuscript are positioned on the leading strand template. The templates were linearised by digestion with AhdI before replication to avoid confounding effects of converging replisomes on circular replication templates. Upon replication initiation on the parental control substrate, two replication forks proceed from the origin in either direction, generating one longer leading strand product of 8.2 kb, and one shorter leading strand product of 1.5 kb. However, if the replisome stalls at a structure-forming sequence, a 3 kb band appears at the expense of the longer 8.2 kb leading strand product (Fig EV1). Lagging strand maturation factors have been omitted in these experiments. Therefore, lagging strand products remain as Okazaki fragments and run as a smear on denaturing agarose gels (Fig 1B, lane 1).

As expected, the replicated control template generated two major leading strand products (8.2 and 1.5 kb) and Okazaki fragments

Table 2. Sequences of iM oligonucleotides and their biophysical properties. Melting and annealing temperature and their hysteresis measured via UV spectroscopy, data shown as Mean ± SD (n = 3), italic temperatures are less prominent, however, present. CD spectroscopy determined transitional pH, error ± 0.1. Thermal difference spectra profiles DNA structural signature.

		UV melting and annealing			CD	TDS
Substrate	**Sequence (5′ -> 3′)**	**T_M (°C)**	**T_A (°C)**	**Hysteresis (°C)**	**pH_T**	**Structure**
AC017019.1	CCCCCCTCCCCCCCTCCC CCCTCCCCCC	51.1 ± 0.0	47.4 ± 0.6	3.7 ± 0.6	7.0	i-Motif
DAP	CCCCCGCCCCCGCCCCCG CCCCCGCCCCC	47.8 ± 0.6	44.8 ± 0.6	3.0 ± 0.0	5.9	i-Motif
		25.6 ± 4.3	*13.5 ± 1.5*	*12.1 ± 3.6*	7.1	
PIM1	CCCCCGACGCGCCCCCCA ACACACAAACCCCCAGAAT CCGCCCCC	49.4 ± 1.5	27.4 ± 1.2	22.0 ± 1.7	6.6	i-Motif
		35.1 ± 0.7		*7.7 ± 1.8*		
ZBTB7B	CCCCCCATCCCTCCCCTCC CTCCCCCCGCCCCTGCCA CCCCCCAAACTCCCCCCC CCC	49.2 ± 1.0	38.3 ± 1.2	9.3 ± 0.6	6.7	i-Motif
DUX4L22	CCCCCGAAACGCGCCCC CCTCCCCCCTCCCCCCTC TCCCCC	38.0 ± 0.0	27.4 ± 0.5	10.7 ± 0.5	6.9	i-Motif
DUX4L22 MUT	CCTCCGAAACGCGCCTTC CTCCTTCCTCCTTCCTCTC CTCC	15.4 ± 0.0	11.4 ± 0.0	4.0 ± 0.0	6.3	i-Motif
		25.7 ± 0.5		*14.3 ± 0.5*		
SNORD112	CCCCCCCCCGCCCCCCA CCCCCCCACCCCCCCCC CC	38.1 ± 0.0	30.1 ± 0.0	8.0 ± 0.0	7.1	i-Motif
SNORD112 MUT	CCTCCTTCCGCCTTCCAC CTTCTCACCTCCTCCTCC	25.4 ± 0.0	12.4 ± 0.0	13.0 ± 0.0	5.5	i-Motif
		17.1 ± 0.5		*4.1 ± 0.5*	6.6	
MYCPu22 rev comp	TTACCCACCCTACCCAC CCTCA	7.7 ± 0.5	> 5.0	> 2.0	5.9	i-Motif
GGGT rev comp	ACCCACCCACCCACCC	9.0 ± 0.3	> 5.0	> 4.0	5.8	i-Motif

(Fig 1B, lane 1). In contrast, a faint but reproducible 3 kb band appeared in the presence of some of the G4-forming sequences tested, indicating replisome stalling (Fig 1B, lanes 2–8). The efficiency of replication reactions is inherently variable between different experiments and different templates. This can result in variability in the stalling intensities observed for any given sequence. To account for this, the intensity of the 3 kb stall band is quantified from three independent experiments and normalised to the intensity of the 1.5 kb band (Fig EV2A). A thermal difference spectrum (TDS) was obtained for each sequence to observe the characteristic G4-profile (data not shown). The thermal stability of the G4s was assessed via UV–vis melting, which revealed a positive

Figure 1. A single G4 or iM structure stalls the replisome.

A Schematic of replication templates used in this study. Position of the origin of replication is marked as 'ori' from which replication initiates. The multiple cloning site (indicated by a red star) is positioned 3 kb downstream of the origin and was used to insert various G4 or iM-forming sequences into the template.

B, C *In vitro* replication reactions using linear substrates containing individual G4-forming sequences (B) or i-Motif-forming sequences (C). Products were analysed by denaturing gel electrophoresis. Bottom panel shows increased contrast of the region containing the 3 kb stall band indicated by the dashed box to better visualise stall products.

D Replication reactions of linear substrates containing *wildtype* or mutated G4 sequences depicted in Appendix Fig S1A. Wildtype sequences are indicated in green and mutated sequences are indicated in red. Products are visualised on a denaturing agarose gel. *P* values to determine statistical significance between replication stalling at *wildtype* versus mutated sequences were calculated by Mann–Whitney tests and were as follows: c-MYC versus c-MYC MUT = 0.2, $(GGGT)_4$ versus $(GGGT)_3$ = 0.1, CEB25 L111(T) versus CEB25 L111(A) = 0.4.

E Quantification of stalling intensities of substrates as in (D) from three independent experiments. Stalling intensities are normalised to the intensity of 'leading strand 2' in each lane, and the mean ± standard error is plotted.

F Analysis of replication products of linear *wildtype* iM substrates or mutated versions containing two consecutive repeats as shown in Appendix Fig S1B on a denaturing agarose gel. Wildtype sequences are indicated in blue and mutated sequences are indicated in red. *P* values to determine statistical significance between replication stalling at *wildtype* versus mutated sequences were calculated by Mann–Whitney tests and were as follows: $(DUX4L22)_2$ versus $(DUX4L22\ MUT)_2$ = 0.2, $(SNORD112)_2$ versus $(SNORD112\ MUT)_2$ = 0.1.

G Quantification of stalling intensities induced by substrates as depicted in (F) from three independent experiments. 3 kb stall band intensities were normalised to the intensity of the 1.5 kb 'leading strand 2' product to account for variation in reaction efficiencies. Mean is plotted, and error bars represent standard error of the mean.

Source data are available online for this figure.

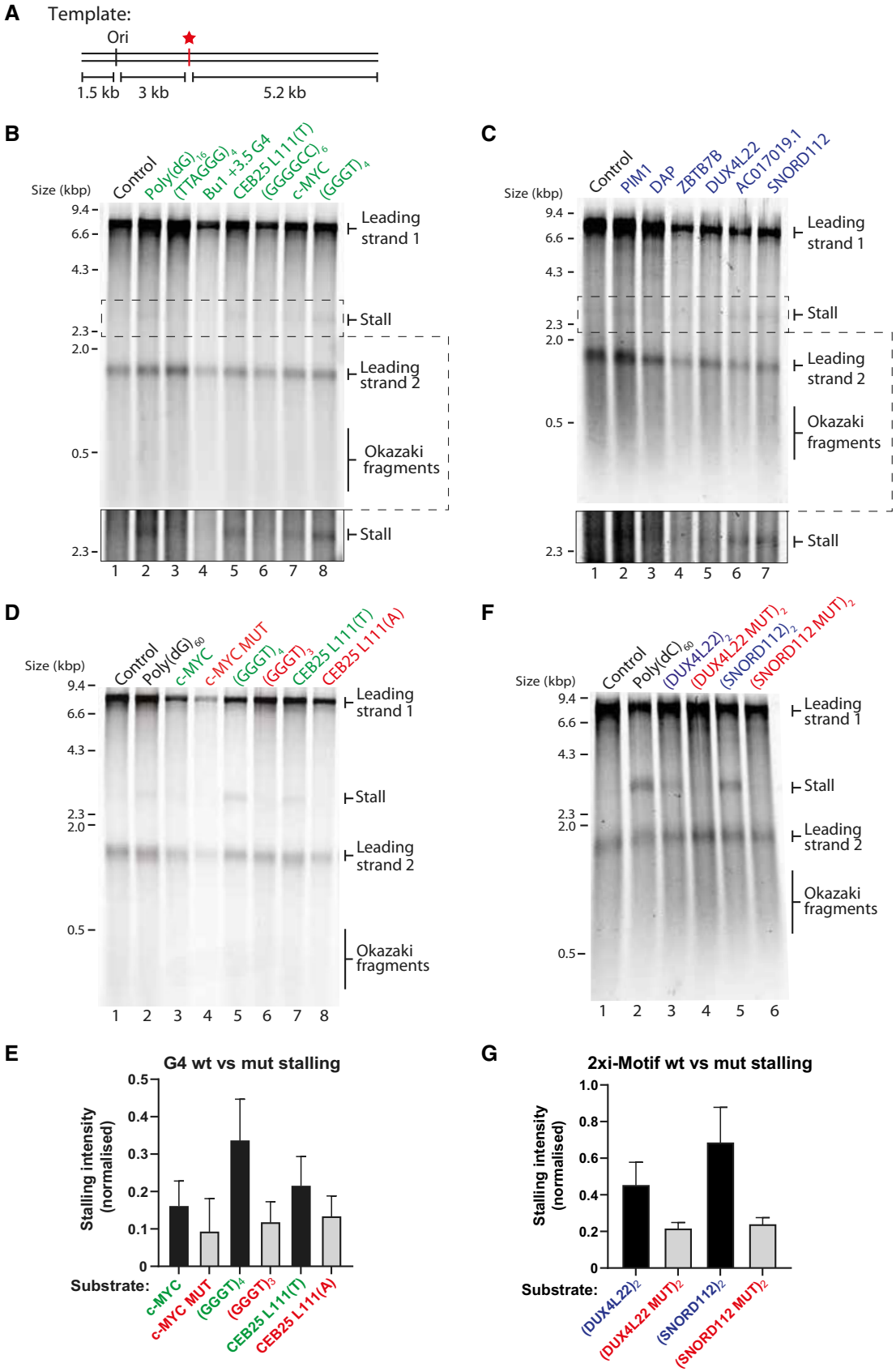

Figure 1.

correlation between melting temperature (T_m) and stalling intensity, with a Pearson correlation *r* value of 0.76 (Fig EV2B). This is highlighted in Table 1, which depicts the melting temperatures of G4s. Some of the G4s we tested, such as $(GGGGCC)_6$, could not be assigned a melting temperature due to aggregation issues, likely due to formation of multimolecular structures. Similarly, poly$(dG)_{16}$ could not be accurately characterised. These sequences were therefore excluded from further studies.

Replication stalling was also reproducibly induced by a range of physiologically derived single iM sequences, although to a lesser degree than G4s (Figs 1C and EV2C). In contrast to G4s, the intensity of replication stalling by iMs did not correlate with their relative thermal stability (Fig EV2D). Rather, there was a weak positive correlation between iM stalling and their transitional pH (pH_T) (Fig EV2E, Table 2).

Stalling is dependent on structure formation

To test the hypothesis that stalling is due to structure formation, we introduced mutations that abrogate or disrupt structures (Appendix Fig S1A and B). These included removing a G-tract from $(GGGT)_4$ to produce $(GGGT)_3$ and mutating the central guanine in each G-tract of *c-MYC* Pu22 to adenine. As an intermediate experiment, we mutated the loop regions in CEB25 L111(T) from thymine to adenine residues, which still allows for G4 formation but reduces its thermal stability (Piazza *et al*, 2015). Consistent with our hypothesis, we saw a consistent, though not statistically significant, reduction in stalling with the mutated sequences (Fig 1D and E). The reduction in stalling was less significant for CEB25 L111 (A), likely because it can still form a structure, albeit weaker. Importantly, biophysical characterisation demonstrated that these sequences either form weak structures, or none at all (Table 1). As expected, the melting temperatures of the mutated G4 sequences were reduced relative to the wildtype sequences (Appendix Fig S1C), resulting in a positive correlation between stalling and thermal stability (Appendix Fig S1E, Pearson correlation *r* value of 0.7). Although the melting temperature for CEB25 L111(A) remained relatively high as it was still able to form a G4, the stalling intensity was reduced when compared to CEB25 L111(T), which is consistent with its weakened thermal stability (Fig 1D and Appendix Fig S1C). Testing the effect of mutations on individual iM-forming sequences was challenging as stalling at a single iM was generally weaker than that observed at a single G4. We therefore tested the effect of two consecutive iMs and observed stronger replisome stalling (Fig 1F), which permitted analysis of mutants. When the iM-forming sequences DUX4L22 and SNORD112 were disrupted for their structure-forming ability (Appendix Fig S1B), stalling was consistently reduced, albeit not statistically significantly so (Fig 1F and G). This was less evident for DUX4L22, which is reflected in the fact that the mutations have a greater effect on the transitional pH and thermal stability of SNORD112, with a small effect on DUX4L22 (Appendix Fig S1D, F, and G; Table 2).

Replisome stalling is dependent on the probability of structure formation

Stalling induced by a single G4- or iM-forming sequence was reproducible, although relatively weak when compared to other types of structure-prone repeats (Casas-Delucchi *et al*, 2022). Larger arrays of consecutive quadruplex-forming sequences may exacerbate replisome stalling. To test this, we replicated templates containing an increasing number of consecutive G4 or iM-forming sequences (Fig 2A and B) and found that stalling increased with the number of structure-forming sequences (quantified from three independent experiments in Fig EV3A and B). Intriguingly, upon replication of iM sequences, a novel 5 kb replication product accumulated (Fig 2B). Although this product was sometimes weakly visible with G4-forming sequences, it was consistently prominent upon replication of iMs. This product corresponds to the length of leading strand 1 from the site of the structure-forming sequence downstream to the end of the template (Fig EV1). This could either be a result of intrinsic repriming events, or DNA breakage at the site of the iM. We investigate these possibilities later.

The observed increase in stalling with arrays of quadruplex-forming sequences could either be due to formation of multiple concurrent structures within the same molecule, or due to increased likelihood of structure formation. We noted that poly$(dG)_{60}$, which could in theory form up to four G4 structures, induced more robust stalling than 16 consecutive G4-forming sequences (Figs 2A and EV3A). In the case of an uninterrupted tract of guanines, a G4 could form from any guanines within the sequence. This is in contrast to other distinct G4-forming sequences we tested (Fig 2A), where structure formation is constrained to a defined window of G-tracts. These observations suggest that in addition to structure stability

Figure 2. Replisome stalling is dependent on probability of structure-formation and is affected by orientation.

A Replication of G4 substrates containing poly$(dG)_{60}$ or an increasing number of consecutive (*c-MYC* Pu22)$_n$ or $(GGGT)_n$ repeats. Products were analysed on a denaturing agarose gel.

B Replication of iM substrates containing poly$(dC)_{60}$ or an increasing number of consecutive (DUX4L22)$_n$ or (SNORD112)$_n$ repeats. Products were analysed on a denaturing agarose gel.

C Replication of substrates containing a tract of poly$(dG)_{60}$, either uninterrupted (lane 2), interrupted every 5th guanine with either a thymine or adenine, or interrupted every 10th guanine with either a thymine or adenine. Replication products were analysed on a denaturing agarose gel.

D Replication of substrates containing a tract of poly$(dC)_{60}$, either uninterrupted, interrupted every 5th cytosine with either an adenine or thymine, or interrupted every 10th cytosine with either an adenine or thymine. Replication products were analysed on a denaturing agarose gel.

E Replication products from substrates containing a tract of poly$(dG)_{60}$, or arrays of either (c-MYC Pu22)$_8$ or $(GGGT)_{28}$ on the leading strand template in the forward (F) or the reverse orientation (R). In the forward orientation, the G-rich strand serve as a template for leading strand synthesis, where in the reverse orientation, the C-rich strand serves as a leading strand template.

F Replication products from substrates containing a tract of poly$(dC)_{60}$, or arrays of $(DAP)_4$, $(DUX4L22)_4$, or $(SNORD112)_4$ on the leading strand template in the forward (F) or the reverse orientation (R).

Source data are available online for this figure.

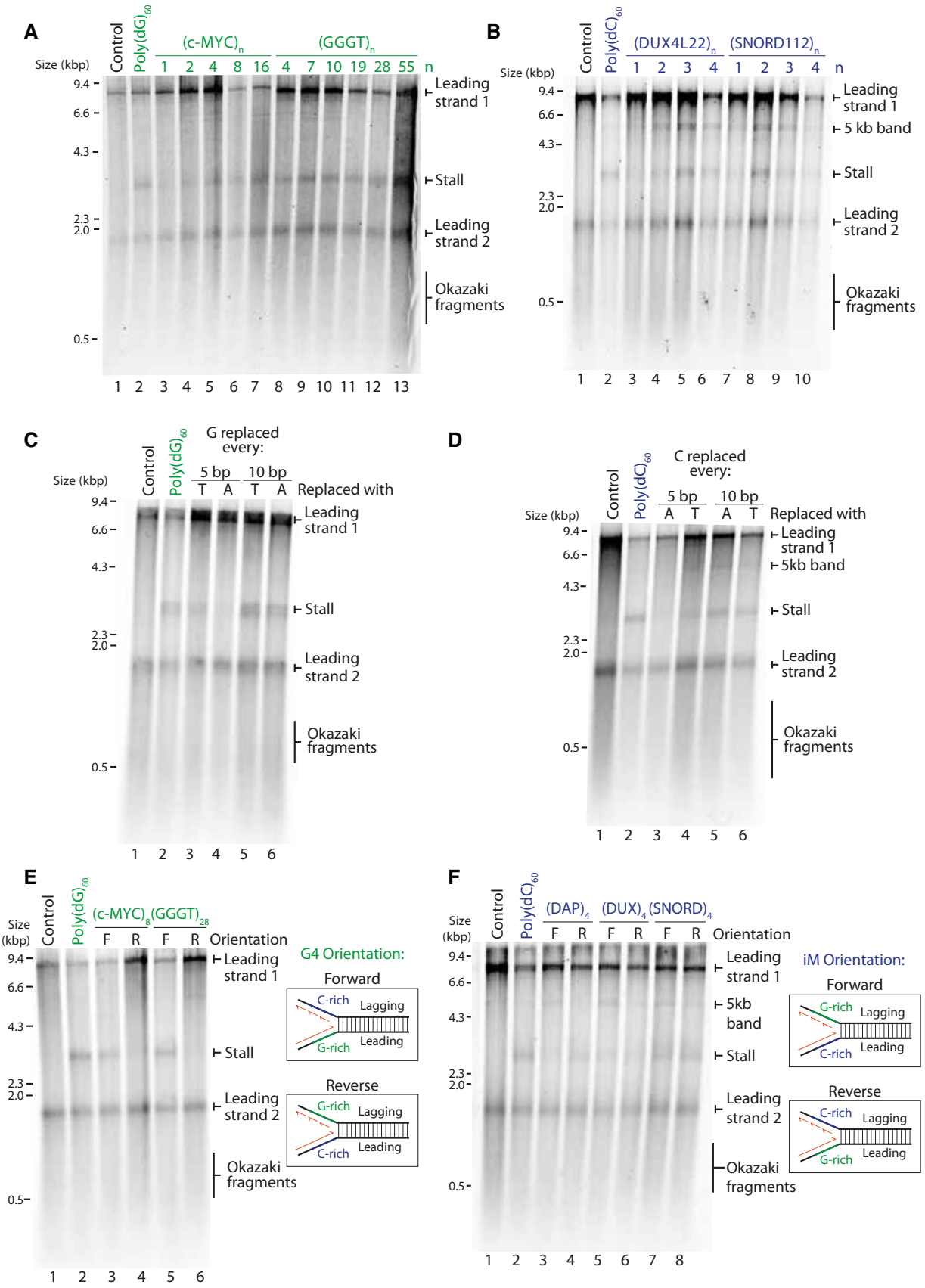
A
Control
Poly(dG)60
(c-MYC)n
(GGGT)n
1 2 4 8 16 4 7 10 19 28 55 n
Size (kbp)
9.4
6.6
4.3
2.3
2.0
0.5
Leading strand 1
Stall
Leading strand 2
Okazaki fragments
1 2 3 4 5 6 7 8 9 10 11 12 13
B
Control
Poly(dC)60
(DUX4L22)n
(SNORD112)n
1 2 3 4 1 2 3 4 n
Size (kbp)
9.4
6.6
4.3
2.3
2.0
0.5
Leading strand 1
5 kb band
Stall
Leading strand 2
Okazaki fragments
1 2 3 4 5 6 7 8 9 10
C
Control
Poly(dG)60
G replaced every:
5 bp 10 bp
T A T A
Replaced with
Size (kbp)
9.4
6.6
4.3
2.3
2.0
0.5
Leading strand 1
Stall
Leading strand 2
Okazaki fragments
1 2 3 4 5 6
D
Control
Poly(dC)60
C replaced every:
5 bp 10 bp
A T A T
Replaced with
Size (kbp)
9.4
6.6
4.3
2.3
2.0
0.5
Leading strand 1
5kb band
Stall
Leading strand 2
Okazaki fragments
1 2 3 4 5 6
E
Control
Poly(dG)60
(c-MYC)8(GGGT)28
F R F R Orientation
Size (kbp)
9.4
6.6
4.3
2.3
2.0
0.5
Leading strand 1
Stall
Leading strand 2
Okazaki fragments
G4 Orientation:
Forward
C-rich
Lagging
G-rich
Leading
Reverse
G-rich
Lagging
C-rich
Leading
1 2 3 4 5 6
F
Control
Poly(dC)60
(DAP)4 (DUX)4 (SNORD)4
F R F R F R Orientation
Size (kbp)
9.4
6.6
4.3
2.3
2.0
0.5
Leading strand 1
5kb band
Stall
Leading strand 2
Okazaki fragments
iM Orientation:
Forward
G-rich
Lagging
C-rich
Leading
Reverse
C-rich
Lagging
G-rich
Leading
1 2 3 4 5 6 7 8

Figure 2.

(Fig 1), stalling efficiency is also dictated by the probability of secondary structure formation. To test this possibility, we interrupted the poly$(dG)_{60}$ sequence such that it could still support G4-formation but constrained to specific G-tracts. Leading strand stalling was reduced when the sequence was interrupted, and this was more prominent when interruptions were more frequent (Fig 2C, compare lane 2 to lanes 3 and 4 and Fig EV3C). Interrupting the poly$(dC)_{60}$ tract produced similar results (Figs 2D and EV3D). We conclude that stalling efficiency is determined not only by structure stability but also by the probability of structure formation.

Having established that replication is stalled due to a quadruplex-forming sequence on the leading strand template, we next sought to determine how a quadruplex-forming sequence on the lagging strand template affects leading strand replication. To this end, we cloned G4-forming sequences in the forward orientation (leading strand template) or reverse orientation (lagging strand template) and observed leading strand replication products (Fig 2E). It is important to note that although we have cloned structure-forming sequences on the lagging strand template (reverse), we did not include factors required for Okazaki fragment maturation, and as such we only observed the effects on leading strand replication. While leading strand stalling was observed when the G4-forming sequence was in the forward orientation, no stalling was seen when in the reverse orientation (Fig 2E, compare lanes 3 and 5 to lanes 4 and 6). Although we did not analyse lagging strand synthesis, previous work has demonstrated that the replication machinery skips over a lagging strand G4, resulting in a small gap, about the size of an Okazaki fragment, on the nascent lagging strand (Kumar *et al*, 2021).

We performed similar experiments to determine how an iM-forming sequence on the lagging strand template affects leading strand synthesis. Interestingly, leading strand stalling occurred in both orientations (forward and reverse) (Fig 2F). Given the shorter consensus sequence of stable G4s relative to iMs, we speculate that the stalling observed in the reversed orientation in this scenario is due to G4 formation by the complementary G-rich sequence on the leading strand template. In contrast, the C-rich sequences which are complementary to the G4-forming sequences in Fig 2E are not able to form very stable iM structures (Table 2, both have a low pH_T ~5.8). This may explain why we do not observe leading strand replication stalling when these sequences are positioned on the leading strand template (Fig 2E, lanes 4 and 6).

CMG can eventually bypass a pre-formed G-quadruplex structure

Having observed consistent replisome stalling at quadruplex-forming sequences, we next wanted to determine whether the stall was transient or persisted over time. To determine this, we carried out pulse-chase experiments, where newly synthesised DNA is labelled with radiolabelled dATP for 10 min, after which an excess of unlabelled dATP is added. This prevents labelling of newly initiating replication forks and allows specific analysis of forks that have initiated in the first 10 min of the reaction. Replication forks stalled at G4 and iM-forming sequences were not resolved over time and persisted for up to 2 h (Fig 3A). This persistent arrest could either be due to blocked unwinding by the CMG helicase or lack of synthesis by polymerase ε. To address the first possibility, we carried out unwinding assays to determine the ability of CMG to unwind pre-formed G4 or iM structures. We chose sequences which induced the strongest replisome arrest – namely $(GGGT)_4$ and $(SNORD112)_1$, as well as mutated versions which abrogate structure formation (Table EV1). These sequences were located on the translocating strand. To favour structure formation, we inserted a poly$(dT)_{19}$ stretch on the opposite strand (Batra *et al*, 2022). Consistent with previous work (Kumar *et al*, 2021), time course analysis revealed that CMG unwinding was initially inhibited by a G4 structure, evident within the first 5–10 min of the reaction (Fig 3B). This was particularly evident when compared to a G4 mutant sequence (Fig 3C), duplex (Appendix Fig S2A) or bubble (Appendix Fig S2B). However, inhibition of unwinding was not terminal, and CMG was able to eventually unwind G4 substrates to levels similar to the G4 mutated substrate (Fig 3B and C). Interestingly, an iM structure had little effect on CMG unwinding (Fig 3D and E). We observed that unwinding of mutated G4 and iM sequences was slightly less efficient than fully duplexed and bubble substrates (compare Fig 3C and E to Appendix Fig S2A and B). This may be due to interspersed contacts between adenine residues in the mutated sequences and the poly $(dT)_{19}$ loop. To bypass a pre-existing quadruplex structure, CMG may either dismantle the structure or 'hop' over and leave it intact. To distinguish between these possibilities, we assessed the effect of a G4-stabilising ligand, PhenDC3 (De Cian *et al*, 2007). If CMG 'hops' over G4s, stabilising them should have no effect. In contrast, if CMG directly unwinds structures, further stabilising a G4 will inhibit unwinding. In the presence of a low concentration of PhenDC3 (0.25 μM), we observed little effect on duplex (Fig 3F) and G4 mutant unwinding (Appendix Fig S2C). In contrast, unwinding of the G4 substrate was inhibited (Fig 3G). Therefore, CMG bypasses pre-existing G4 structures by dismantling them rather than 'hopping' over them.

Replication templates do not contain pre-formed secondary structures

All the evidence gained thus far indicates that secondary structures are the cause for replication stalling. However, it was not clear whether structures were pre-formed (for example during

Figure 3. The response of CMG to pre-formed quadruplexes.

A Pulse-chase time course experiment with (*c-MYC* Pu22)$_4$ or (SNORD112)$_4$ substrates. Reactions were initiated with radiolabelled dATP for 10 min, chased with excess 'cold' dATP and samples taken at the indicated time points.

B–E CMG unwinding assays on substrates containing a pre-formed G4 (B), a mutant G4 (see Table EV1) (C), pre-formed iM (D) or a mutant iM (see Table EV1) (E). CMG unwinding was stimulated by the addition of 2 mM ATP following CMG loading in the presence of ATPγS. Samples were taken at the indicated time points. Products were run on 10% TBE gels. Input and boiled substrates were used as controls to visualise where original and unwound substrates migrate. The proportion of template unwound was calculated by measuring the intensity of the 'unwound' product band as a proportion of the total product intensity for each lane.

F, G CMG unwinding assays on duplexed substrates (F) or substrates containing a pre-formed G4 (G). Reactions were carried out as in (B–E) but with the addition of 0.25 μM PhenDC3 where indicated.

Source data are available online for this figure.

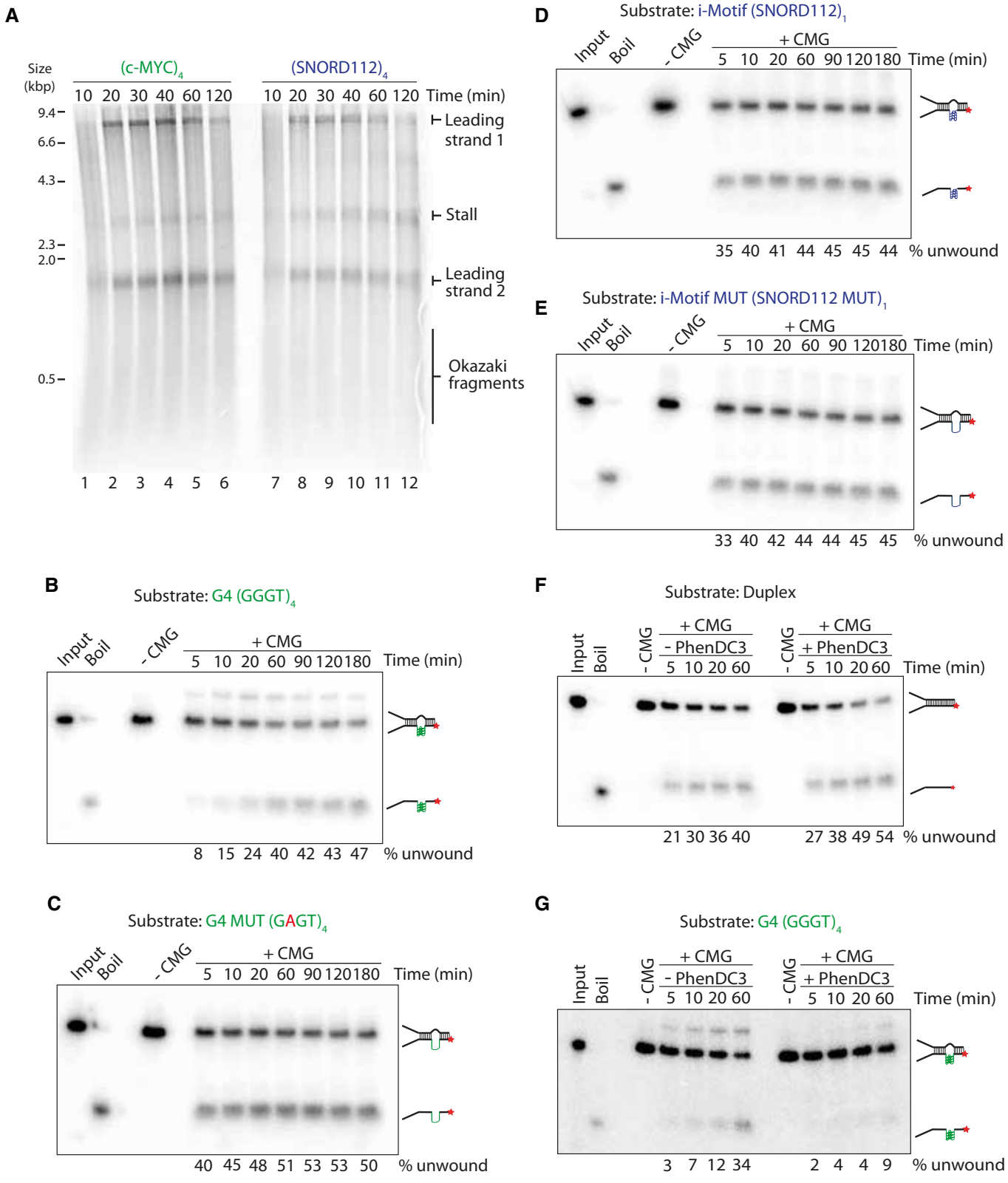

Figure 3.

propagation in bacteria) or were generated during replication. To directly determine whether our replication templates contain pre-existing structures, we employed solid-state nanopore sensing, which was recently utilised to detect quadruplex structures in double-stranded DNA (Boskovic *et al*, 2019). A positive control contained a single G-quadruplex at a predefined asymmetric

position along a dsDNA molecule (Boskovic *et al*, 2019). DNA is passed through the nanopores and the ionic current measured. Folded G4s give rise to a variation in topology relative to dsDNA that in turn produces a characteristic signal in the ionic current (Fig EV4A). The DNA molecule can enter the nanopore in any orientation, which would place the G4 either proximal or distal (Fig EV4B and C). Besides current drops indicative of G4s, we also observe larger peaks that can be attributed to naturally occurring DNA knots (Fig 4A, 'knot'). The random position and frequency (~10%) of these knots is within the expectation for DNA molecules of this length (Plesa *et al*, 2016).

The summary scatterplot of the peak positions in the first 100 informative events from our nanopore measurement of the positive control is shown in Fig 4B (top panel). Virtually all events include a G4 structure (99/100) within the expected relative positions of 0.2 and 0.8. We observed a smaller proportion of naturally occurring knots, randomly distributed along the DNA molecules. Importantly, in the absence of potassium ions, only knots were detected with no discernible G4 signals (Fig 4B, bottom panel).

Having established these positive and negative controls, we next measured our replication substrates, with secondary structures expected at relative positions 0.3 and 0.7 (Fig EV4D and E). In contrast to the positive control, none of the replication substrates produced detectable quadruplex peaks. Rather, all substrates, including the empty control, exhibited random knots with a similar distribution and frequency (Figs 4C and EV4F). We conclude that our replication substrates do not contain any pre-existing structures.

Replisome stalling at G4s leads to helicase-polymerase uncoupling

As we had observed that our replication templates do not contain any pre-formed structures and that CMG can directly unwind such structures, we inferred that they must be forming as a consequence of replication. We hypothesised that structures forming behind CMG inhibit synthesis by polymerase ε, while CMG continues to unwind downstream. This phenomenon, termed helicase-polymerase uncoupling, occurs in response to various leading strand DNA damage lesions (Taylor & Yeeles, 2018) and other types of repetitive sequences (Kumar *et al*, 2021; Casas-Delucchi *et al*, 2022) and leads to the exposure of ssDNA. To determine if the same response occurs at G4-forming sequences, we utilised a previously established approach whereby an exogenous primer complementary to the region 264 nt downstream of the G4 sequence is added to the reaction (Taylor & Yeeles, 2018; Casas-Delucchi *et al*, 2022). This primer can only anneal if ssDNA is exposed, leading to restart of DNA synthesis, thereby serving as a readout for helicase-polymerase uncoupling. As shown in Fig 4D, addition of this primer led to the appearance of 5 kb restart products for all G4-forming sequences tested, but these were not seen with a scrambled primer. This restart product was absent from the empty vector (Fig 4D, lane 1) but was evident with a template containing a CPD lesion (Fig 4D, lane 3), which served as a positive control. This is strong evidence that unwinding by the CMG helicase continues beyond the G4 sequence, but synthesis by polymerase ε is inhibited. Analysis of the mechanism of stalling at iM sequences using this method is more complex, due to the presence of the intrinsic 5 kb band. However, the facts that CMG can unwind past an iM (Fig 3D), and our substrates do not contain any pre-existing structures (Fig 4C), suggest that stalling within iMs is also due to inhibition of DNA synthesis by pol ε, which most likely also results in helicase-polymerase uncoupling at iM-forming sequences.

Given that our substrates do not contain any pre-formed secondary structures (Fig 4C), we considered the possibility that structures arise on the ssDNA template exposed by CMG unwinding. If this were true, then increasing the amount of ssDNA would enhance the likelihood of structure formation and consequently result in more polymerase stalling. Exposure of excess ssDNA is typically limited as polymerase ε is thought to be tightly coupled to CMG through a direct interaction (Zhou *et al*, 2017). As polymerase ε is essential for replication initiation, it cannot be omitted from replication reactions. However, deletion of its catalytic domain, which completely eliminates its polymerase activity, is compatible with replication initiation. Under these conditions, polymerase δ carries out leading strand synthesis. Since polymerase δ does not directly interact with CMG, this results in discontinuous synthesis that is not coupled to unwinding. Replication reactions with this polymerase ε mutant resulted in increased replisome stalling when compared to the wildtype protein (Fig 4E, compare odd lanes to even lanes). This was true for both G4 and iM-forming sequences. We conclude that replication fork uncoupling leads to enhanced fork stalling and propose that this occurs due to increased probability of secondary structure formation.

Replication products break at i-Motifs

Upon replication of substrates containing iM-forming sequences, we consistently observed the presence of a novel 5 kb product on

Figure 4. Secondary structures are not pre-formed and likely arise as a result of replication, leading to helicase-polymerase uncoupling.

A Schematic of a positive control DNA passing through the nanopore in the direction that positions the G4 proximally and a representative nanopore measurement event with a DNA knot in the middle of the molecule. The G-quadruplex structure and its corresponding current drop are marked in blue. The DNA knot and its corresponding current drop are marked in green. Numbers indicate the proportion through the DNA the G4 is positioned.

B Summary scatterplots of the peak positions in the first 100 informative nanopore events for the positive control (where K^+ is added) and the negative control (no K^+ present). The negative control does not contain any G-quadruplex structure without the presence of potassium ions. Numbers indicate proportion of G4s or knots in 100 unfolded events.

C Nanopore measurement results of the first 100 informative nanopore events for replication templates. Summary scatterplots of the peak positions are shown for an empty control and substrates containing (*c-MYC* Pu22)$_{16}$ or (SNORD112)$_4$. Numbers indicate proportion of G4s or knots in 100 informative events.

D Replication reactions carried out on G4-containing templates in the presence of a primer that anneals 264 nt downstream of the G4 (rp) or a scrambled control primer (scr).

E Replication of G4 or iM substrates with either *wildtype* pol ε (wt) or a pol ε mutant with a deleted catalytic domain (Δcat). Products were analysed on a denaturing agarose gel.

Source data are available online for this figure.

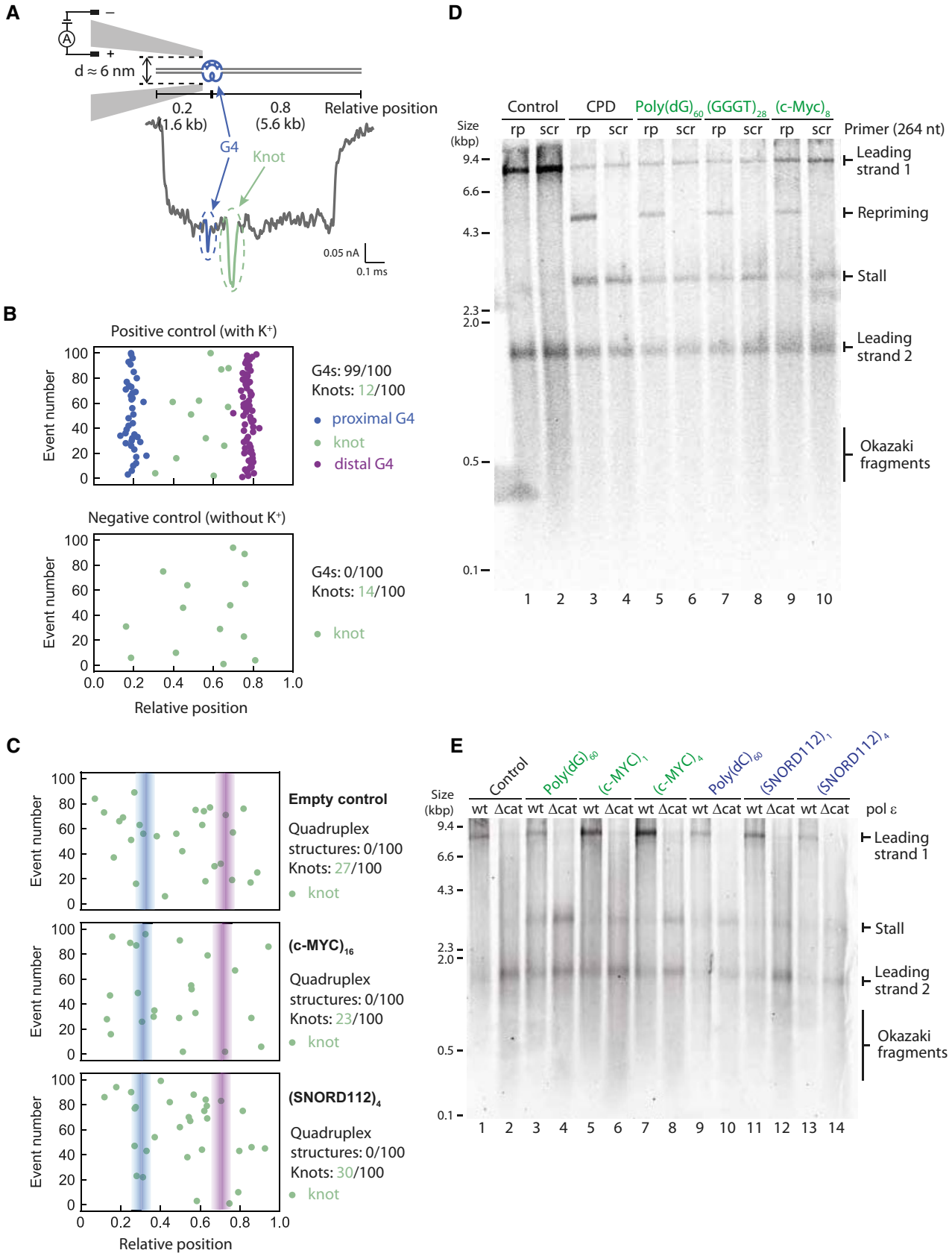

Figure 4.

denaturing gels, as highlighted previously. We hypothesised that these products may arise as a result of either re-priming or DNA breakage at the site of the iM during or after replication (Fig EV1). To address the latter possibility, we simulated broken replication products by digesting fully replicated control templates post-replication with an enzyme that cleaves within the insert (Fig 5A). The resulting product harbours a double-stranded break at the position of the iM on newly synthesised DNA. To simplify analysis and reduce the heterogeneity in product length arising as a result of flaps generated by strand displacement, polymerase δ was excluded from these reactions. We verified that this novel 5 kb band was unaffected by the presence of polymerase δ (Appendix Fig S3C). Upon analysis by native gel, we observed that the smaller population of products generated by iM substrates migrated at the same positions as the simulated 'broken products' (Fig 5B, compare lanes 2 and 3 to lane 4).

To further analyse these broken replication products, we carried out two-dimensional (2D) gel electrophoresis. As expected, analysis of replication products of an iM template demonstrated the presence of stalled forks and incompletely replicated forks in the population of replication intermediates (Fig 5C). Full-length products consisted mostly of full-length leading strands 1 and 2 and Okazaki fragments. 2D gel analysis maps the 5 kb band to the products identified on the native dimension as broken (Fig 5C). We also observed a weaker population of products in the denaturing dimension corresponding to the second faster migrating broken product on the native gel (Fig 5C). Importantly, these bands mapped to the same positions observed with the simulated broken products (Fig 5D), were absent from the empty vector (Fig EV5A) and were also observed with a different iM-forming sequence (Fig EV5B). Together, these results suggest that replication induces breakage within iMs. We note that we cannot discount that in addition to these broken products, some intrinsic repriming events also occur (Fig EV1), which would generate products that migrate as full-length on the native dimension but may be masked by the strong signal of leading strand 1 (Fig 5C).

Stalling at quadruplexes can be rescued by a specialised helicase

Having established the mechanism of fork stalling within quadruplexes, we next wanted to understand how replisomes minimise or resolve stalls. Since increased fork uncoupling enhanced replisome stalling (Fig 4E), we considered the possibility that improved coupling might reduce stalling. CTF18-RFC is an alternative PCNA clamp-loader to the canonical RFC1-RFC that has been proposed to increase coupling of DNA synthesis and unwinding by directly binding polymerase ε (Grabarczyk *et al*, 2018; Stokes *et al*, 2020). However, addition of CTF18-RFC, in the absence or presence of RFC1-RFC, did not affect stalling at either G4s or iMs (Appendix Fig S3A).

Previous work from our laboratory had revealed that polymerase δ, as well as high concentrations of dNTPs, can rescue stalling at hairpin-forming sequences, but not at poly$(dG)_n$ or poly$(dC)_n$ (Casas-Delucchi *et al*, 2022). Consistent with this, polymerase δ was not able to rescue stalling at any G4 (Appendix Fig S3B) or iM-forming sequence (Appendix Fig S3C). Similarly, an excess of any dNTP alone, or in combination, was not able to resolve stalling at either G4 (Appendix Fig S4A) or iM (Appendix Fig S4B) forming sequences. We considered the possibility that the relative ratio of dNTPs may be more important than their absolute concentration. This raised the prediction that an increased proportion of dCTP relative to dA/dG/dTTP might be able to rescue stalling at G4-forming sequences. However, stalled forks were not rescued by a further excess of dCTP (2-fold over dATP and 26-fold over dGTP and dTTP (Appendix Fig S4C)). Altogether, this suggests that once the replisome stalls at a quadruplex-forming sequence, the stall is persistent and cannot be overcome by replisome-intrinsic mechanisms.

We previously found that Pif1 could rescue forks stalled at poly$(dG)_n$ and poly$(dC)_n$ sequences (Casas-Delucchi *et al*, 2022), raising the possibility that it could rescue stalling at all quadruplex-forming sequences. Pif1 is a well-characterised G4-unwinding helicase shown to play a vital role in enabling the efficient replication of G4s both *in vivo* and *in vitro* (Ribeyre *et al*, 2009; Lopes *et al*, 2011; Paeschke *et al*, 2011, 2013; Byrd *et al*, 2018; Dahan *et al*, 2018; Sparks *et al*, 2019b; Maestroni *et al*, 2020). However, there are additional helicases that bind and unwind G4 structures both *in vitro* and *in vivo*, such as Rrm3, Sgs1, Hrq1 and Chl1. Rrm3 is another yeast Pif1-family helicase with a high sequence and functional similarity to Pif1 (Bessler *et al*, 2001). Like Pif1, Rrm3 is a 5′-3′ helicase which has overlapping functions with Pif1 and helps the replisome bypass barriers such as at tRNA promoters and telomeric DNA (Ivessa *et al*, 2002, 2003). Sgs1 is a 3′-5′ RecQ family helicase shown to preferentially unwind G4 DNA and is the yeast homologue of the BLM and WRN helicases (Huber *et al*, 2002). Similarly, Hrq1 is the yeast homologue of another RecQ helicase, RecQ4. RecQ4 is one of the five RecQ helicases found in humans, with 3′-5′ polarity. It functions in telomere maintenance (Ghosh *et al*, 2012) and has been shown to bind and unwind G4 structures (Rogers *et al*, 2017). Chl1 is the yeast homologue of human ChlR1 (also called DDX11). ChlR1 is a 5′-3′ helicase that directly unwinds G4 structures and is proposed to help process G4s during DNA replication (Wu *et al*, 2012; Lerner *et al*, 2020). To test the role of these helicases, we carried out pulse-chase experiments by pulsing for 10 min, during which a persistent stall occurred at G4 or iM-forming sequences. We then added a candidate helicase and allowed replication to continue for a further 10 min to determine if the stall could be resolved. Since Chl1 is recruited to replisomes via an interaction with Ctf4

Figure 5. Replication products break at i-Motifs.

A Schematic of replication products arising from replication of a control template (top), a control template digested with NotI post-replication to simulate 'broken products' (middle), and an iM template where potential product breakage occurs at the site of the iM (indicated by a red star) (bottom).

B Analysis of control or iM-containing replication products on a native gel. 'Broken products' was generated by replication of a control template and post-reaction digestion with NotI which cleaves the product at the site of the insert.

C, D Two-dimensional (2D) gel electrophoresis of replication products of an iM-containing template (C) or a 'broken products' control (D) (as described in A). Replication products were run firstly in the native dimension and subsequently in the denaturing. Inset in (C) shows increased contrast of the region containing the broken products as indicated by the dashed box.

Source data are available online for this figure.

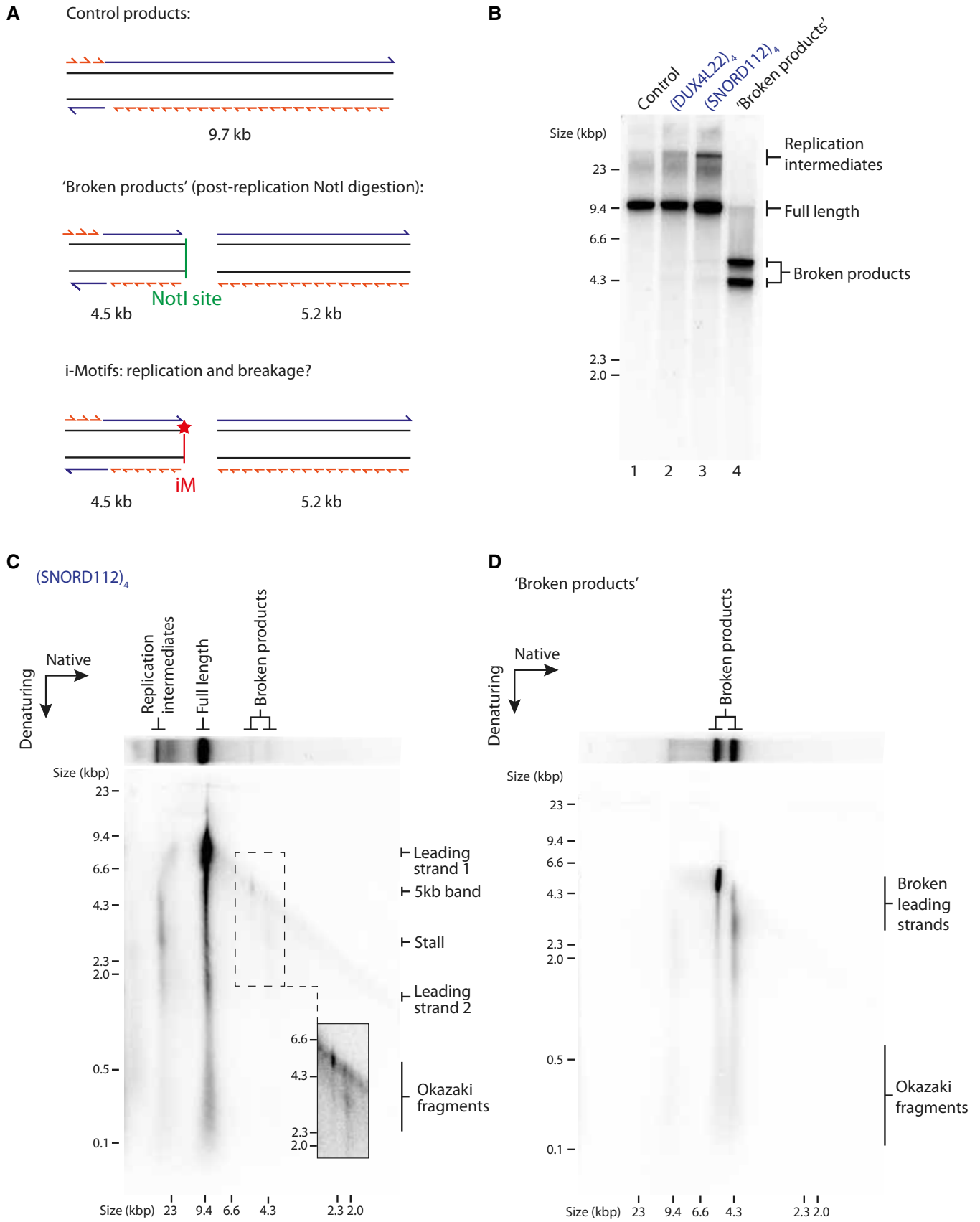

Figure 5.

(Samora *et al*, 2016), we also included Ctf4 in our experiments with Chl1. Neither Sgs1 (Appendix Fig S5A and B), Chl1 (Appendix Fig S5C and D), Rrm3 (Appendix Fig S5E), nor Hrq1 (Appendix Fig S5F) were able to rescue stalling at either G4 or iM-forming sequences. Importantly, these enzymes were active on model substrates, although Rrm3 and Hrq1 displayed only partial unwinding activity (Appendix Fig S5G–J). In contrast, and in agreement with our previous work, Pif1 was able to rescue forks stalled at both G4s and iMs (Fig 6A and B). The extent of rescue was less evident for expanded sequences such as $(GGGT)_{28}$ and $(SNORD112)_4$ which may indicate that consecutive G4 or iM structures pose a greater challenge to Pif1. Rescue was dependent on the helicase activity of Pif1, as no rescue was observed with the Pif1 ATPase mutant K264A. The fact that Pif1, but not other implicated helicases, was able to rescue forks stalled at quadruplex-forming sequences demonstrates its specificity, and highlights that only specialised helicases are able to resolve fork stalling at G4 and iM sequences.

Discussion

We have assessed the response of the eukaryotic replisome to a variety of G4 and iM-forming sequences and found that a single quadruplex-forming sequence alone is able to stall DNA replication. This is a significant finding as these classes of sequences are highly prevalent in the human genome. Current estimates are between 370,000 (Huppert & Balasubramanian, 2005, 2007) and ~700,000 (Chambers *et al*, 2015) G4-forming sequences and 5,125 iM-forming sequences (Wright *et al*, 2017). These must all be replicated accurately to maintain genome integrity. Importantly, we found that the encounter of a replisome with a single quadruplex forming sequence can lead to the same mechanistic response as triggered in response to DNA damage. Moreover, in addition to inducing fork stalling, iMs have the propensity to induce DNA breakage. This raises the possibility that there are many physiological DNA sequences within the human genome that have the potential to threaten genome stability through distinct mechanisms.

The ability of a G4-forming sequence to stall DNA replication correlates with its structure-forming potential. Consistent with this, mutated sequences that cannot form structures do not impact replisome progression. Together, these observations provide strong evidence that it is a G4 structure that causes replication stalling, and not the sequence itself. Importantly, we have characterised the effects of iMs on replisome progression. Here, we observed consistent replisome stalling at a variety of physiological iM sequences. Although the response of the replisome to iMs appears largely similar to G4s, we do observe some differences. First, replication stalling at iMs was generally weaker than that observed at G4s. We speculate that this may be because all iMs examined here are weaker structures than those formed by the G4s. This could mean they are less likely to form during replication, although once formed they appear to be a persistent and stable block to replisome progression. Second, the ability of iMs to stall replication seems to be less influenced by melting temperature than G4s and may correlate better with transitional pH. Interestingly, previous studies have found that iMs with a higher transitional pH have a higher potential for iM formation *in vivo* and in turn are more likely to undergo mutations and deletions in human cells (Martella *et al*, 2022). Moreover, the biophysical characterisation of these sequences was done on short oligonucleotides, and the actual thermal stability of these structures within the context of duplexed DNA may in fact be higher. Still, the fact that these structures are more influenced by pH than G4s may explain why we observe a weaker stall in our assays carried out under physiological pH conditions. The fact that stalling occurs in our *in vitro* system under physiological pH strongly supports the idea that iMs are indeed able to form and can be a robust block to the replisome, highlighting their biological relevance.

Importantly, we have observed that iMs can also induce DNA breakage. This is a significant finding as this has the potential to threaten genome stability if not repaired correctly. How and when this DNA breakage occurs in the context of replication remains to be seen. Although we have obtained evidence that a proportion of replication products break at iMs, we cannot rule out the possibility that endogenous re-priming may occur preferentially at iM-forming sequences. All primases use a purine to initiate primer synthesis and therefore require a pyrimidine on the template strand. As such, polymerase α has been suggested to prime preferentially at CCC sequences (Davey & Faust, 1990). This may be a mechanism to preserve DNA integrity downstream of forks stalled at iMs, as has been suggested by polymerase α and the 9-1-1 complex downstream of forks stalled at G4s (van Schendel *et al*, 2021). Another possibility is that the broken products we observe are a consequence of stall-driven repriming events, which somehow promote breakage at iMs. We cannot distinguish whether breakage occurs after unperturbed replication or after stalling and repriming, as both events would yield identical products.

Single molecule solid-state nanopore experiments demonstrate that our substrates do not contain any significant levels of pre-formed structures. Therefore, secondary structures must be forming during replication, resulting in inhibition of synthesis by polymerase ε. As ssDNA is the precursor for structure formation, we favour a model whereby structures form on ssDNA exposed behind the CMG helicase (Fig 6C). This is consistent with a recent super-resolution microscopy study which detected the presence of G4 structures between the CMG helicase and either PCNA or nascent DNA (Lee *et al*, 2021). Although CMG and polymerase ε are usually tightly

Figure 6. Pif1 rescues stalling at both G4s and iMs.

A, B Pulse-chase experiments carried out with the indicated templates. Reactions were initiated with radiolabelled dATP. After a 10 min pulse, either *wildtype* or ATPase-dead K264A (mut) Pif1 was added with the chase and samples taken after another 10 min.

C Model illustrating the effects of G4s and iMs on replication. CMG unwinds past a leading strand quadruplex-forming sequence and secondary structures form from the exposed ssDNA. These structures inhibit synthesis by polymerase ε, leading to helicase-polymerase uncoupling. Pif1 can unwind both G4s and iMs and allow synthesis to resume. iMs can be resolved in this manner or lead to nascent DNA breakage in the absence or presence of a repriming event. Lagging strand products may remain intact.

Source data are available online for this figure.

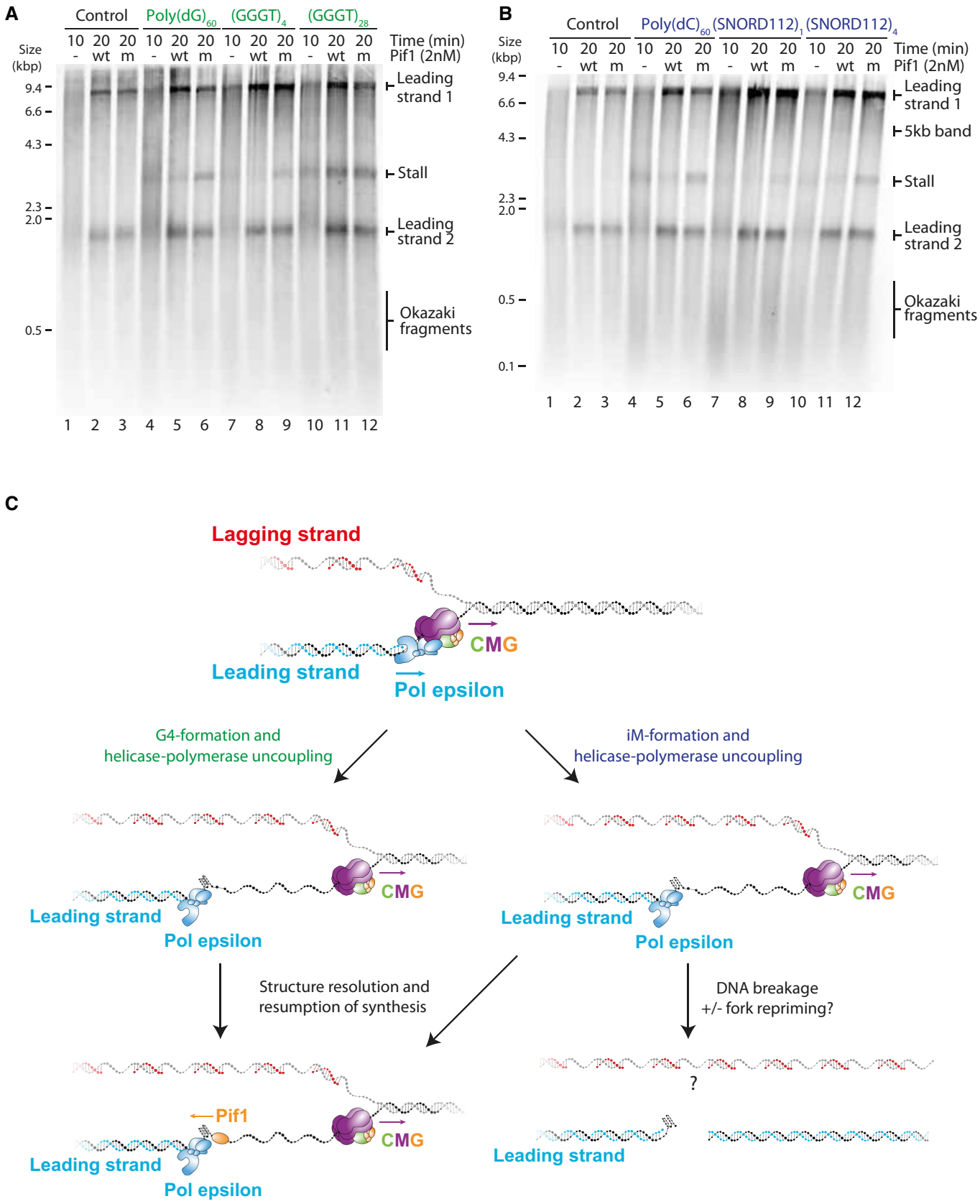

Figure 6.

coupled in the replisome, the length of ssDNA running between the exit channel of CMG and the active site of polymerase ε is unknown. The most recent structural models of the eukaryotic replisome suggest a gap of at least 16-nt (Yuan *et al*, 2020). This would be sufficient ssDNA to allow G4 formation, or to nucleate iM formation.

Although we observed consistent replisome stalling at G4 and iM-forming sequences, we never observed a complete block to all replication forks and only saw a proportion of replication forks stalling. This was true even in the presence of up to 16 consecutive G4-forming sequences. Therefore, a major determinant of replication fork stalling is the likelihood of structure formation. This explains why we observed only a marginal increase in the proportion of replication forks stalling with an increasing number of consecutive G4s or iMs. In the presence of a larger number of structure-forming repeats, a structure is more likely to fold due to sequence availability, but once a single structure has formed it is sufficient to block the replisome, and additional structures downstream would have no additional effect on synthesis. Similarly, the fact that we consistently observed a greater proportion of replication forks stalling at poly $(dG)_{60}$ and poly$(dC)_{60}$ may be because a structure can form in any given window and is not constrained by loop sequences. This is consistent with previous biophysical characterisations of poly$(dC)_n$ sequences, which found that the optimum transitional pH peaks at poly$(dC)_{28}$ and gets lower as the number of cytosines increases (up to poly$(dC)_{40}$) (Fleming *et al*, 2017). This suggests that iM structures formed by longer tracts of cytosines are not inherently more stable, but rather are more likely to fold. However, once formed, this structure is a robust block to the replisome that cannot be resolved by any replicative polymerase. In addition, structures which fold more quickly may be more likely to fold and in turn stall replication. There are known differences in the kinetics of folding between the two different iM topologies, the 3′ E and 5′ E conformations, which are distinguished by the position of the outermost C:C^+ base pair. In the human telomeric iM structure, it has been shown that the 3′ E conformation forms faster but this may not be necessarily applicable for all iMs and will depend on the sequences within the loop regions (Malliavin *et al*, 2003; Lieblein *et al*, 2013). Folding kinetics usually correlate with structure stability, which may also contribute to the fact that both structure stability and probability of formation play a role in inducing replication stalling. In addition to the dynamics of the structure itself, the dynamics of how tightly each replication fork is coupled will determine whether there is sufficient time and space for structures to form.

In some cases, G4s and iMs can form on complementary strands of the same sequence. In a physiological context, a stable G4 requires four tracts of three guanines. However, the complementary C-rich sequence would not form a stable iM at a physiological pH. Therefore, a stable G4 does not necessarily equate to a stable iM on the opposite strand. However, a stable iM requires four tracts of five cytosines at a physiological pH (Wright *et al*, 2017). The complementary G-rich sequence would conform to the requirement of a stable G4, and as such it is more conceivable that a stable G4 structure would be found opposite an iM. This may explain why we observed an orientation-dependent stalling for G4s, but an orientation-independence for iMs.

Similar to our previous work with repetitive sequences (Casas-Delucchi *et al*, 2022), we observe uncoupling between helicase unwinding and DNA synthesis in response to quadruplexes. This is consistent with previous work which demonstrates an enrichment of G4-forming sequences within 6 kb of uncoupled forks in tumour cells (Amparo *et al*, 2020). This response is akin to the response to leading strand DNA damage (Taylor & Yeeles, 2018) and leads to the exposure of ssDNA. In a physiological context, exposure of large amounts of ssDNA as a result of replication stress can lead to the activation of checkpoint pathways (MacDougall *et al*, 2007). Further studies are required to explore if such processes occur in response to G4s and iMs during replication. The ssDNA exposed during replisome uncoupling can also be a substrate for recombination and mutation events, which may explain why G4s and iMs are frequent mutation hotspots and undergo rearrangements (Lopes *et al*, 2011). A recent high-throughput primer extension assay using T7 DNA polymerase demonstrated that polymerase stalling at structure-prone sequences generates point mutations with a higher frequency than slippage events. Consistent with their higher propensity to inhibit synthesis, G4s displayed higher mutation rates than iMs and were often mutated in the loop regions (Murat *et al*, 2020). Whether this same phenomenon occurs with eukaryotic polymerases in the context of the complete replisome remains unclear. Many of these structure-forming sequences have been found at cancer mutation hotspots or breakpoints (De & Michor, 2011; Wang & Vasquez, 2017; Bacolla *et al*, 2019), and replication stalling could be a potential explanation for mutational events. Indeed, DNA breakage at iMs may directly contribute to their mutagenic potential in cancer.

We have demonstrated that CMG is able to bypass a G4 or iM sequence and established that synthesis by polymerase ε is inhibited. Stabilisation of G4 structures using a small molecule inhibited unwinding by CMG, suggesting that CMG bypasses a G4 by dismantling the structure as opposed to 'hopping' over the structure and leaving it intact. This is in contrast with its ability to bypass intact DNA-protein cross-links (Sparks *et al*, 2019a), leading strand oxidative lesions (Guilliam & Yeeles, 2021) and lagging strand blocks (Langston *et al*, 2017). It remains to be seen whether replisome stalling occurs in the same position each time. Higher resolution studies could map the position of replisome stalling within the G4 or iM and decipher whether the replisome consistently stalls at the base of the structure, or if it is able to progress some distance through.

It is unsurprising that we observe rescue of replication fork stalling at G4s by Pif1, given the breadth of data describing its role as a G4-unwinding helicase (Ribeyre *et al*, 2009; Lopes *et al*, 2011; Paeschke *et al*, 2011, 2013; Byrd *et al*, 2018; Dahan *et al*, 2018; Sparks *et al*, 2019b; Maestroni *et al*, 2020). However, the fact that Pif1 is also able to resolve forks stalled at iMs points towards the broad specificity of Pif1 as a helicase. This is in line with its ability to also resolve forks stalled at hairpins (Casas-Delucchi *et al*, 2022). Our observation that rescue of replisome stalling was less efficient with an array of consecutive G4 and iM sequences may indicate that multiple structures are formed within these arrays, which may require more extensive helicase activities.

Interestingly, none of the other helicases tested were able to rescue fork stalling at G4s or iMs, despite their demonstrated ability to unwind G4s (Huber *et al*, 2002; Wu *et al*, 2012; Rogers *et al*, 2017). One potential explanation could be unwinding polarity. Pif1 unwinds 5′ to 3′, while some of the other helicases exhibit 3′ to 5′ activity. Our working model is that exposure of ssDNA downstream of the G4 or iM allows accessibility to helicases with 5′ to 3′ activity, but not to those with 3′ to 5′. Another possible explanation could be

preference for certain types of G4s. For example, Chl1 has been shown to have stronger unwinding activity on anti-parallel G4s (Wu *et al*, 2012), while the G4 sequences we tested all form parallel G4s, which is a more common conformation. Similarly, the fact that Rrm3 was unable to rescue stalling at G4s despite its relation to Pif1 may reflect the fact that these helicases often have different functions despite binding the same substrates (Bessler *et al*, 2001). This may also explain the large number of quadruplex-unwinding helicases that appear to have some level of redundancy, as they may each have a role in resolving structures in different scenarios. For example, BLM helicase has been shown to suppress recombination at G4s in transcribed genes (van Wietmarschen *et al*, 2018). The fact that only an accessory helicase was able to resolve stalls at G4s and iMs may also explain why mutations in helicases such as these lead to genome instability diseases, such as Bloom's Syndrome (reviewed in Cunniff *et al*, 2017), Werner's syndrome (Yu *et al*, 1996) and Fanconi Anaemia (reviewed in Brosh & Cantor, 2014).

Recent advances in the field have provided the tools to reconstitute human DNA replication *in vitro* (Baris *et al*, 2022). Although the core replication machinery is conserved from budding yeast to human, it remains to be seen whether G4s and iMs have the same impact on progression of the human replisome. Using this system to study replication of structure-forming sequences would also enable one to study the roles of other human proteins in this process, such as an array of human helicases including RecQ helicases such as BLM (Sun *et al*, 1998) and WRN (Fry & Loeb, 1999), RTEL1 (Barber *et al*, 2008; Vannier *et al*, 2013) and the Fanconi Anaemia protein FANCJ (Wu *et al*, 2008).

Altogether, we discovered that a range of physiological G4 and iM structures arising as a result of DNA replication can stall the eukaryotic replisome. This study provides further insight as to why these sequences pose a barrier to DNA replication and suggests a potential mechanism for structure formation and resolution during replication. Moreover, we have found that i-Motifs can directly cause DNA breakage. We therefore propose that endogenous DNA secondary structures are a source of replication stress, which may explain their genomic instability and mutation frequencies in cancer.

Materials and Methods

Constructing repeat-containing replication substrates

Substrates for replication assays were constructed by inserting repetitive sequences into a 9.8 kb parental plasmid (pGC542) containing a single synthetic yeast replication origin (ARS306), which has been previously described (Casas-Delucchi *et al*, 2022). Repetitive sequences were cloned into the MCS 3 kb downstream of the origin and expanded using a strategy that employs synthetic oligos and type IIS restriction enzymes (Scior *et al*, 2011). All oligos were ordered from Integrated DNA Technologies (IDT), the sequences of which can be found in Table EV1.

Preparing templates for replication assays

Plasmids (Table EV2) were transformed into NEB Stable Competent *E. coli* cells (#C3040I), which are ideal for propagation of repeat-containing plasmids. Cultures were grown at 30°C to reduce potential recombination and mutation events. Plasmids were purified using a QIAGEN HiSpeed Maxi Kit. Subsequently, supercoiled plasmids were isolated from nicked plasmids by PlasmidSelect clean up. DNA samples were diluted 6-fold in 100 mM Tris–HCl (pH 7.5), 10 mM EDTA and 3 M $(NH_4)_2SO_4$ (final concentration = 2.5 M) before incubation with 300 µl PlasmidSelect Xtra slurry (pre-washed with 100 mM Tris–HCl (pH 7.5), 10 mM EDTA and 2.3 M $(NH_4)_2SO_4$) for 30 min to bind. Following binding, nicked plasmids were eluted initially with 1 ml buffer consisting of 100 mM Tris–HCl (pH 7.5), 10 mM EDTA and 1.9 M $(NH_4)_2SO_4$. This was repeated twice. Then, 1 ml buffer was added to the beads and allowed to incubate for 10 min at RT. Subsequently, supercoiled plasmids were eluted with 100 mM Tris–HCl (pH 7.5), 10 mM EDTA and 1.5 M $(NH_4)_2SO_4$ by incubation for 10 min at RT. This was repeated once. Samples were de-salted by dialysis against 0.1 × TE for 3 h and overnight. DNA was concentrated using a 100 kDa Amicon concentrator followed by ethanol precipitation and resuspended in 1xTE.

CPD substrate

The substrate containing a site-specific DNA damage (CPD lesion) was prepared as has been previously described (Casas-Delucchi *et al*, 2022).

Protein purification

All protein expression strains, and expression and purification steps were carried out as previously described (Casas-Delucchi *et al*, 2022).

CMG

Saccharomyces cerevisiae CMG was expressed from the budding yeast strain yJCZ3 (Zhou *et al*, 2017). All purification steps were carried out as previously described (Baretic *et al*, 2020), with the following exceptions. After elution from Calmodulin Sepharose 4B (GE Healthcare), the eluate was applied to a MonoQ 5/50 GL column (GE Healthcare) equilibrated in 25 mM Tris–HCl pH 7.2, 10% glycerol, 0.005% TWEEN 20, 0.5 mM DTT, 150 mM KCl. The protein was eluted with a 20 CV gradient from 150 to 1,000 mM KCl and peak fractions were dialysed overnight against 500 ml 25 mM HEPES-KOH pH 7.6, 40 mM KOAc, 40 mM K-glutamate, 2 mM Mg (OAc)2, 0.25 mM EDTA, 0.5 mM DTT, 40% glycerol. The protein was subsequently concentrated through a 0.5 ml 30 K MWCO Pierce™ Protein Concentrator (Thermo Scientific, 88502), snap-frozen and stored at −80°C.

Pol ε-Δcat

The DNA polymerase ε mutant with a deleted catalytic domain (Pol ε-Δcat) was expressed from the budding yeast strain yAJ25, which has been previously described (Yeeles *et al*, 2017), and purified as per wildtype pol ε.

Rrm3

Purified recombinant yeast Rrm3 was expressed and purified as previously described (Deegan *et al*, 2019).

Sgs1

Purified recombinant yeast Sgs1 was expressed and purified as previously described (Cejka & Kowalczykowski, 2010).

Hrq1

Purified recombinant yeast Hrq1 and the catalytic mutant K318A was expressed and purified as previously described (Rogers *et al*, 2017).

Chl1

Chl1 expression strain

Y5562 MAT**a**, ade2-1, ura3-1, his3-11,15, trp1-1, leu2-3,112, can1-100, pep4::HIS3, ade2::ADE2-pRSII402-Gal4-pGal1/10-Chl1- FLAG-Protein A.

Chl1 purification

Budding yeast cells overexpressing Chl1 were grown in YP medium containing 2% raffinose as the carbon source to an optical density of 1.0 at 30°C. 2% galactose was then added to the culture to induce the protein expression, and the cells were further grown for 90 min. Cells were collected by centrifugation, washed with deionised water and suspended in Chl1 buffer (50 mM Tris–HCl pH 7, 10% glycerol, 2 mM $MgCl_2$, 0.5 mM TCEP) containing 0.1% Triton X-100, 500 mM NaCl, 0.5 mM Pefabloc, as well as the cOmplete-EDTA protease inhibitor cocktails. The cell suspension was frozen in liquid nitrogen, then cells were broken in a cryogenic freezer mill. The cell powder was thawed on ice, and further Chl1 buffer containing 0.1% Triton X-100 and 500 mM NaCl, and protease inhibitors was added. The lysate was clarified by centrifugation at 20,000 *g* for 1 h. The clarified lysate was transferred to pre-equilibrated IgG agarose beads. 8 μg/ml RNase A (Merck) was added, and incubated for 2 h. The resin was washed with Chl1 buffer containing 0.1% Triton X-100 and 500 mM NaCl and then incubated in Chl1 buffer containing 0.1% Triton X-100, 500 mM NaCl, 10 mM $MgCl_2$ and 1 mM ATP for 15 min. The resin was washed again with Chl1 buffer containing 0.1% Triton X-100 and 500 mM NaCl and incubated overnight in the same buffer containing 10 μg/ml PreScission protease. The eluate was collected, and Chl1 dilution buffer (50 mM Tris–HCl pH7, 10% glycerol, 2 mM $MgCl_2$, 0.5 mM TCEP, 10 mM NaCl) was added to adjust the salt concentration to 160 mM NaCl. The diluted sample was loaded onto a HiTrap Heparin (Cytiva) column, equilibrated with Chl1 buffer containing 160 mM NaCl. The column was developed with a linear gradient from 160 mM to 1 M NaCl in Chl1 buffer. The peak fractions were pooled and loaded onto a Superdex 200 Increase (Cytiva) gel filtration column that was equilibrated and developed with Chl1 gel filtration buffer (20 mM Tris–HCl pH 7.5, 150 mM NaCl, 10% Glycerol, 0.5 mM TCEP). The peak fractions were concentrated by ultrafiltration.

RFC-Ctf18

RFC-CTF18 expression strain: yEF4

MATa ade2-1 ura3-1 his3-11,15 trp1-1 leu2-3,112 can1-100
bar1::Hyg
pep4::KanMX
ura3::URA3pRS306/Rfc2, CBP-Rfc3
trp1::TRP1pRS304/Rfc4, Rfc5
his3::HIS3pRS303/Ctf18
leu2::LEU2pRS305/Ctf8, Dcc1

Expression and purification steps were carried out as per RFC purification (Casas-Delucchi *et al*, 2022).

In vitro replication assays

MCM loading was carried out for 10 min at 24°C on 3 nM circular DNA that was linearised during loading with 0.3 μl AhdI in a buffer containing 25 mM HEPES (pH 7.6), 10 mM magnesium acetate, 100 mM potassium glutamate, 1 mM DTT, 0.01% NP-40-S, 0.1 mg/ml BSA, 80 mM potassium chloride, 5 mM ATP, 20 nM ORC, 45 nM Cdc6, 75 nM Cdt1-Mcm2-7 and 50 nM DDK. Loading was stopped by the addition of 120 nM S-CDK for 5 min at 24°C. Following loading, samples were diluted in a buffer containing 25 mM HEPES (pH 7.6), 10 mM magnesium acetate, 100 mM potassium glutamate, 1 mM DTT, 0.01% NP-40-S, 0.1 mg/ml BSA to dilute the final contribution of chloride to 14 mM. A nucleotide mix was added to give final concentrations of 200 μM ATP, CTP, GTP and UTP; 30 μM dATP, dCTP, dGTP and dTTP; and 132 nM α-P^{33}-dATP. Subsequently, to initiate replication, a master mix of proteins was added to give final concentrations of 100 nM GINS, 10 nM S-CDK, 10 nM Mcm10, 40 nM Csm3/Tof1, 20 nM Pol ε, 30 nM Dpb11, 40 nM Cdc45, 40 nM Mrc1, 60 nM RPA, 40 nM RFC, 120 nM PCNA, 5 nM Pol δ, 50 nM Pol α, 20 nM Sld3/7 and 20 nM Sld2. Reactions were incubated at 30°C for 40 min. For samples to be run on denaturing gels, 0.5 μl SmaI was added to each 10 μl reaction in the final 10 min of the reaction, which cleaves products approx. 100 bp from the origin of replication. This removes heterogeneity in the length of leading strand products arising due to variability in the exact location where synthesis of leading strands begins, despite origin specificity (Taylor & Yeeles, 2018). Reactions were quenched by adding EDTA to a final concentration of 100 mM.

Pulse-chase experiments were carried out as previously described (Casas-Delucchi *et al*, 2022). During the pulse, unlabelled deoxyribonucleotide concentrations were as follows: 30 μM dCTP, dTTP, dGTP and 2.5 μM dATP. To carry out the chase, unlabelled dATP was added to a final concentration of 400 μM, with the addition of 400 μM of dGTP, dCTP or dTTP, or 800 μM dCTP where indicated.

Repriming experiments were carried out by the addition of 60 nM oligonucleotide after loading and before initiation of replication (Casas-Delucchi *et al*, 2022).

Post-replication sample processing

For denaturing gels, after quenching with 20 mM EDTA, 1/10 volumes of alkaline loading dye (0.5 M NaOH, 10% sucrose, xylene cyanol in water) was added to samples. Replication products were separated on 0.8% alkaline agarose gels in 30 mM NaOH, 2 mM EDTA at 32 V for 16 h. Subsequently, products were fixed on denaturing agarose gels by incubation in 5% TCA for 40 min at room temperature.

For native gels, replication products were treated with 0.1% SDS and 1/100 volumes of Proteinase K at 37°C for 20 min. DNA was extracted using phenol:chloroform:isoamyl alcohol 25:24:1 (Sigma-Aldrich, P2069) and samples were subsequently passed over illustra MicroSpin G-50 columns (Sigma-Alrich, GE27-5330-02) to remove incorporated nucleotides and exchange the buffer to TE. 6× NEB™ Purple Gel Loading Dye (no SDS) (NEB, B7025S) was added to

samples before separation on a 0.8% agarose/TAE gel in 1xTAE at 30 V for 22 h at 4°C.

For two-dimensional (2D) gel electrophoresis, samples were treated as per native gels and then split equally into two lanes on the same native gel as described above (one lane for analysis and one lane for the second dimension). One lane was excised from the native gel and soaked for 2 × 1 h in alkaline running buffer. Gel slices were then horizontally inserted into the top of a 0.8% alkaline agarose gel and run as per standard denaturing gels.

Gels were dried before being exposed to a Storage Phosphor Screen (GE Healthcare, BAS-IP MS 2025) and imaged on a Typhoon scanner (Cytiva). Images were analysed and quantified in ImageJ. Quantifications of stalling intensities were calculated from an average of three replicates in separate experiments. To calculate intensities, the background for each lane was subtracted from each measurement. The 3 kb stalling intensity band was normalised to the intensity of 'leading strand 2' in each lane to account for variation in the efficiencies of reactions for each substrate.

Preparing templates for helicase assays

Forked DNA substrates were prepared as previously described (Batra *et al*, 2022). Briefly, dried oligos from IDT were resuspended to 10 μM in 10 mM Tris pH 8.0. The bottom strand of the substrate (GC340, SW051 or SW105) was end labelled with γ-^{32}P-ATP in a reaction containing 5 pmol oligo, 1× PNK buffer, 1 U of PNK enzyme (NEB, M0201S), and γ-^{32}P-ATP (0.03 mCi). The reaction was incubated for 1 h at 37°C, followed by heat inactivation of PNK for 20 min at 80°C and then 10 min at 90°C. Unincorporated radiolabelled nucleotides were removed by passing the sample through a G50 column (GE Healthcare, 2753002) equilibrated in 10 mM Tris pH 8.0. The concentration of K^+ was then adjusted to 50 mM by the addition of 1 M KOAc. To anneal the complementary top strand (GC339 or SW114), 1 μl of a 10 μM stock of oligonucleotide was added and the reaction was incubated at 95°C for 5 min, followed by a slow cooling to 10°C at a rate of −1°C/min. Annealed products were run on 10% TBE gels (ThermoFisher Scientific, EC62755BOX) in 0.5xTBE at 150 V for 45 min. Fully annealed substrates were isolated from the gel using a crush-soak method as described in Batra *et al*, 2022.

For Chl1, Sgs1, Hrq1 and Rrm3 unwinding assays, substrates containing a 5′ overhang (for Chl1 and Rrm3) and a 3′ overhang (for Sgs1 and Hrq1) were generated as previously described (Casas-Delucchi *et al*, 2022).

Sequences of all oligonucleotides used to generate helicase unwinding substrates are detailed in Table EV1.

Helicase assays

CMG unwinding assays were carried out using 0.5 nM of labelled substrate and 20 nM of purified CMG. Reactions were assembled in a buffer containing 25 mM HEPES pH 7.6, 10 mM MgOAc, 30 mM NaCl, 0.1 mg/ml BSA and 0.1 mM AMP PNP. Reactions were incubated at 30°C for 30 min to allow CMG to pre-load onto the template, before addition of ATP to a final concentration of 2 mM to stimulate unwinding. At this point, 65 nM of the unlabelled version of the labelled oligo (GC340, SW051, SW069, SW105, SW129 or SW130) was added to trap any unwound oligos and prevent substrate re-annealing. Reactions were incubated at 30°C and time points taken as indicated. Reactions were stopped by the addition of 0.5% SDS and 200 mM EDTA, supplemented with Novex Hi-Density TBE Sample buffer (ThermoFisher Scientific, LC6678) and analysed on 10% Novex TBE gels (ThermoFisher Scientific, EC62755BOX) in 1× TBE at 90 V for 90 min. Gels were exposed to a Storage Phosphor Screen (GE Healthcare, BAS-IP MS 2025) and imaged in a Typhoon (Cytiva). Images were analysed and quantified in ImageJ.

For Chl1, Sgs1 and Rrm3 unwinding assays, reactions were carried out using 0.5 nM of labelled duplex and 50 nM of purified recombinant protein as previously described (Casas-Delucchi *et al*, 2022). For Hrq1 unwinding assays, reactions were carried out in the same manner except 0.1 nM labelled duplex and 100 nM of purified recombinant protein was used and reactions were carried out at 37°C.

Biophysical characterisation of G4 sequences

DNA annealing step

DNA sequences (Table 1) were purchased in their lyophilised form with standard desalting purification from Integrated DNA Technology (IDT) and re-dissolved in MilliQ water to reach a stock concentration of 100 μM. The sequences were then further diluted to 10 μM in the annealing buffer (25 mM HEPES, 10 mM $MgCl_2$, 110 mM KCl/LiCl), heated to 95°C for 15 min and left to slowly cool down to room temperature overnight.

Thermal difference spectra (TDS)

100 μl of each of the 10 μM DNA sequences (annealed as above) was transferred into a High Precision Cell (quartz glass) Light Path 10 mm (HellmaAnalytics) and covered with 200 μl of mineral oil to prevent evaporation. The cuvettes were sealed with a plastic lid and transferred into the Agilent Cary 3500 UV-Vis Multicell Peltier spectrometer. A first scan was run at 25°C (Scan range = 800–200 nm | Averaging time (s) = 0.02 | Data Interval (nm) = 1 | Scan rate (nm/min) = 3,000 | Spectral bandwidth (nm) = 2). The samples were then heated to 95°C and left to equilibrate for 7 min before running a second scan. Each TDS curve was obtained by subtracting the absorbance spectra (25°C) by the absorbance spectra (95°C).

UV–Vis melting curve

100 μl of each of the 10 μM DNA sequences (annealed as above) was transferred into a High Precision Cell (quartz glass) Light Path 10 mm (HellmaAnalytics) and covered with 200 μl of mineral oil to prevent evaporation. The cuvettes were sealed with a plastic lid and transferred into the Agilent Cary 3500 UV–Vis Multicell Peltier spectrometer. The melting curve was obtained by imputing the following parameters (Wavelengths: 295 nm | Averaging time (s) = 0.1 | Spectral bandwidth (nm) = 2) and the heating protocol in Table 3. Data were collected only for stages 5 and 6 for each run.

T_m was extrapolated for each sample by fitting the relative melting curve as shown by Mergny and Lacroix (Mergny & Lacroix, 2003) with the Python script provided by Giacomo Fabrini (Fabrini, 2022).

Biophysical characterisation of i-Motif sequences

Oligonucleotides

DNA sequences (Table 2) were supplied by Eurogentec (Belgium), synthesised on a 1,000 nmol scale and purified by reverse phase

Table 3. Heating protocol for Uv–Vis melting curve of DNA sequences.

Stage	Data interval (°C)	Rate (°C/min)	Temperature start/end (°C)
1	1	5	25/95
2	1	5	95/25
3	1	5	25/95
4	1	5	95/25
5	0.1	0.5	25/95
6	0.1	0.5	95/25

HPLC. All DNA sequences were dissolved in ultra-pure water to give 100 μM final concentrations, which were confirmed using a Nanodrop. For all experiments, ODNs were diluted in buffer containing 10 mM sodium cacodylate and 100 mM potassium chloride at the indicated pH. DNA samples were thermally annealed by heating in a heat block at 95°C for 5 min and cooled slowly to room temperature overnight.

Circular dichroism

CD spectra were recorded on a Jasco J-1500 spectropolarimeter using a 1 mm path length quartz cuvette. ODNs were diluted to 10 μM (total volume: 100 μl) in buffer at pH increments of 0.25 or 0.5 pH units from 4.0 to 8.0, depending on the sequence. Spectra were recorded at 20°C between 200 and 320 nm. Data pitch was set to 0.5 nm and measurements were taken at a scanning speed of 200 nm/min, response time of 1 s, bandwidth of 2 nm and 100 mdeg sensitivity; each spectrum was the average of four scans. Samples containing only buffer were also scanned according to these parameters to allow for blank subtraction. Transitional pH (pH_T) for each iM was calculated from the inflexion point of fitted ellipticity at 288 nm.

UV absorption spectroscopy

UV spectroscopy experiments were performed on a Jasco J-750 equipped with a Julabo F-250Temperature Controller and recorded using low volume masked quartz cuvettes (1 cm path length). Annealed DNA samples (250 μl) were transferred to a cuvette and covered with a stopper to reduce evaporation of the sample. The absorbance of the DNA was measured at 295 nm and 260 nm as the temperature of the sample was held for 10 min at 4°C, heated to 95°C at a rate of 0.5°C per min, then held at 95°C for 10 min before the process was reversed; each melting/annealing process was repeated three times. Data were recorded every 1°C during both melting and annealing and melting temperatures (T_m) were determined using the first derivative method. TDS were obtained by subtracting the spectrum of the folded structure between 220 and 320 nm at 4°C from that of the unfolded structure at 95°C. The data were normalised and maximum change in absorption was set to +1 as previously described (Mergny *et al*, 2005).

Data analysis

Final analysis and presentation of the data was performed using GraphPad Prism version 9.0. All sets of data passed Shapiro–Wilk normality test, *P*-values were calculated by One way ANOVA followed by Holm-Sidak posthoc analysis for the melting temperature and thermodynamic data collected from the triplicate measurements for each oligonucleotide.

Table 4. Detailed sequences of the customised oligonucleotides.

Strand name	Sequence
G16	TTCGACAACTCGTATTAAATCCTTTGCCCG TTTGGGTGGGTGGGTGGGTTTT AAAGTTTGAGTAACATTATCATTTTGCGGA
cG16	AACGTTATTAATTTTA

Nanopore detection of structures

Plasmids for nanopore analysis were pre-linearised at the origin of replication by digestion with SmaI. This generated linear templates with the structure-forming sequence positioned asymmetrically from the ends of the DNA (30% into the template, 70% from the other end of the template). Following digestion, DNA was extracted using phenol:chloroform:isoamyl alcohol 25:24:1 (Sigma-Aldrich, P2069) and subsequently ethanol precipitated and resuspended in ddH_2O.

Synthesis of control DNA molecules

The linear ssDNA scaffold for our designs as the positive control and negative control was obtained by cutting circular M13mp18 DNA (New England Biolabs) at BamHI-HF and EcoRI-HF (New England Biolabs, 100 units/μl) restriction sites following our published protocol (Bell & Keyser, 2016). Staple 42 and staple 43 in the basic staple set (Bell & Keyser, 2016) were replaced by our customised strand G16 with four repeats of GGGT in the middle to form the G-quadruplex secondary structure in the presence of potassium cations. Another strand, cG16, was added to form a double helix with the scaffold at the position where the G-quadruplex formed and thus stabilised the structure. All the DNA oligonucleotides were purchased from Integrated DNA Technologies, Inc. (IDT). Detailed sequences of the customised oligonucleotides can be found in Table 4. After mixing the modified oligonucleotide set and the M13mp18 scaffold at a 5:1 stoichiometric ratio, the solution was heated to 70°C followed by a linear cooling ramp to 25°C over 50 min. Excess oligonucleotides were removed using Amicon Ultra 100 kDa filters. After quantification with Nanodrop 2000 spectrophotometer, samples were then kept in a freezer at −20°C for later measurements.

Nanopore measurement

Nanopores used in this project were fabricated by laser-assisted pulling (P-2000, Sutter Instrument) of quartz capillaries (outer diameter 0.5 mm and inner diameter 0.2 mm, Sutter Instrument) as in our previous work (Bell & Keyser, 2016), though a higher pulling temperature (HEAT = 500) were used to obtain smaller nanopores with diameters of about 6 nm and higher signal-to-noise ratio. Current–voltage characteristic curves from −600 mV to 600 mV were recorded to indicate the estimated sizes and the root-mean-square (RMS) noise of the ionic current through the nanopores. Details can be found in Table 5. Once functional nanopores had been identified, the central reservoir of our nanopore chip was filled with our DNA sample (0.2 nM in 200 mM KCl and 4 M LiCl buffer, except for 0.2 nM in 4 M LiCl buffer when measuring the negative control group). A positive voltage of 600 mV was then applied to drive negatively charged DNA molecules through the nanopore, creating characteristically transient changes in the ionic current trace.

Table 5. Parameters of the nanopores used.

DNA sample	Diameter (nm)	Root-mean-square noise (pA)
Positive control	6.3	6.0
Negative control	5.9	6.3
Empty control	6.3	5.8
16 × Myc	6.0	5.4
55 × GGGT	6.1	5.7
60 × G/C	5.7	6.0
4 × SONRD	6.1	5.7
4 × DUX4L22	5.3	5.6

Data analysis was performed with the LabVIEW software and self-written python programs. It is important to note that a small slope was often observed at the baseline, probably due to the slight change in the buffer concentration as the measurement was carried out. The current baseline was linearly fitted, and the slope was corrected in Figs 4A–C and EV4 for better presentation. When we drew a reference line at 0.15 nA below the current baseline, the two intersections of the reference line and the current trace of one event were taken as its start and end. The event duration Δt_0 is the time-scale between the start and end, and Δt refers to the interval between any second-level peak beyond the first-level plateau and the start (Fig EV4A). The position of the peak is calculated as $Position = \frac{\Delta t}{\Delta t_0}$.

Data availability

This study includes no data deposited in external repositories.

Expanded View for this article is available online.

Acknowledgements
This work was funded by a Wellcome Trust and Royal Society Sir Henry Dale fellowship (210470/Z/18/Z) as well as internal funding from the Institute of Cancer Research. Marco Di Antonio was supported by a Biotechnology and Biological Sciences Research Council (BBSRC) David Phillips Fellowship [BB/R011605/1] and a Lister Prize Fellowship. Federica Raguseo was supported by a Leverhulme Trust, Cellular Bionics scholarship [EP/S023518/1]. Dilek Guneri was supported by a BBSRC grant [BB/W001616/1]. We would like to thank Petr Cejka (Institute for Research in Biomedicine, Switzerland) and Tom Deegan (University of Edinburgh, UK) for providing published purified recombinant proteins. We are thankful to Matthew L. Bochman (Indiana University, USA) for providing constructs for Hrq1 purification. We would like to thank Max Douglas for reagents and experimental support, and Manuel Daza Martin for critical reading of the manuscript. We are thankful to Giacomo Fabrini and Lorenzo Di Michele for support on Tm analysis. U.F.K and Y.L. thank F. Boskovic for help with the design of the G4 control structures and help with sample preparation for the nanopore experiments.

Author contributions
Corella S Casas-Delucchi: Conceptualization; supervision; investigation; methodology; writing – review and editing. **Dilek Guneri:** Investigation; writing – original draft. **Emma E Fletcher:** Resources. **Federica Raguseo:** Investigation; writing – original draft. **Gideon Coster:** Conceptualization; supervision; funding acquisition; investigation; project administration; writing – review and editing. **Joseph TP Yeeles:** Resources. **Marco Di Antonio:** Supervision; funding acquisition; writing – original draft. **Masashi Minamino:** Resources. **Sophie L Williams:** Conceptualization; data curation; formal analysis; investigation; methodology; writing – original draft; writing – review and editing. **Ulrich F Keyser:** Supervision; funding acquisition; writing – original draft. **Yunxuan Li:** Investigation; writing – original draft. **Zoë AE Waller:** Supervision; funding acquisition; writing – original draft.

Disclosure and competing interests statement
The authors declare that they have no conflict of interests.

References

Amparo C, Clark J, Bedell V, Murata-Collins JL, Martella M, Pichiorri F, Warner EF, Abdelhamid MAS, Waller ZAE, Smith SS (2020) Duplex DNA from sites of helicase-polymerase uncoupling links non-B DNA structure formation to replicative stress. *Cancer Genomics Proteomics* 17: 101–115

Bacolla A, Ye Z, Ahmed Z, Tainer JA (2019) Cancer mutational burden is shaped by G4 DNA, replication stress and mitochondrial dysfunction. *Prog Biophys Mol Biol* 147: 47–61

Barber LJ, Youds JL, Ward JD, McIlwraith MJ, O'Neil NJ, Petalcorin MI, Martin JS, Collis SJ, Cantor SB, Auclair M *et al* (2008) RTEL1 maintains genomic stability by suppressing homologous recombination. *Cell* 135: 261–271

Baretic D, Jenkyn-Bedford M, Aria V, Cannone G, Skehel M, Yeeles JTP (2020) Cryo-EM structure of the fork protection complex bound to CMG at a replication fork. *Mol Cell* 78: 926–940

Baris Y, Taylor MRG, Aria V, Yeeles JTP (2022) Fast and efficient DNA replication with purified human proteins. *Nature* 606: 204–210

Batra S, Devbhandari S, Remus D (2022) CMG helicase activity on G4-containing DNA templates. *Methods Enzymol* 672: 233–260

Bell NA, Keyser UF (2016) Digitally encoded DNA nanostructures for multiplexed, single-molecule protein sensing with nanopores. *Nat Nanotechnol* 11: 645–651

Bell SP, Labib K (2016) Chromosome duplication in *Saccharomyces cerevisiae*. *Genetics* 203: 1027–1067

Bessler JB, Torres JZ, Zakian VA (2001) The Pif1p subfamily of helicases: region-specific DNA helicases? *Trends Cell Biol* 11: 60–65

Biffi G, Tannahill D, McCafferty J, Balasubramanian S (2013) Quantitative visualization of DNA G-quadruplex structures in human cells. *Nat Chem* 5: 182–186

Boskovic F, Zhu J, Chen K, Keyser UF (2019) Monitoring G-quadruplex formation with DNA carriers and solid-state nanopores. *Nano Lett* 19: 7996–8001

Brosh RM Jr, Cantor SB (2014) Molecular and cellular functions of the FANCJ DNA helicase defective in cancer and in Fanconi anemia. *Front Genet* 5: 372

Brown RE, Freudenreich CH (2021) Structure-forming repeats and their impact on genome stability. *Curr Opin Genet Dev* 67: 41–51

Byrd AK, Bell MR, Raney KD (2018) Pif1 helicase unfolding of G-quadruplex DNA is highly dependent on sequence and reaction conditions. *J Biol Chem* 293: 17792–17802

Casas-Delucchi CS, Daza-Martin M, Williams SL, Coster G (2022) The mechanism of replication stalling and recovery within repetitive DNA. *Nat Commun* 13: 3953

Catasti P, Chen X, Deaven LL, Moyzis RK, Bradbury EM, Gupta G (1997) Cystosine-rich strands of the insulin minisatellite adopt hairpins with intercalated cytosine+.cytosine pairs. *J Mol Biol* 272: 369–382

Cejka P, Kowalczykowski SC (2010) The full-length *Saccharomyces cerevisiae* Sgs1 protein is a vigorous DNA helicase that preferentially unwinds holliday junctions. *J Biol Chem* 285: 8290–8301

Chambers VS, Marsico G, Boutell JM, Di Antonio M, Smith GP, Balasubramanian S (2015) High-throughput sequencing of DNA G-quadruplex structures in the human genome. *Nat Biotechnol* 33: 877–881

Cunniff C, Bassetti JA, Ellis NA (2017) Bloom's syndrome: clinical spectrum, molecular pathogenesis, and cancer predisposition. *Mol Syndromol* 8: 4–23

Dahan D, Tsirkas I, Dovrat D, Sparks MA, Singh SP, Galletto R, Aharoni A (2018) Pif1 is essential for efficient replisome progression through lagging strand G-quadruplex DNA secondary structures. *Nucleic Acids Res* 46: 11847–11857

Dai J, Carver M, Hurley LH, Yang D (2011) Solution structure of a 2:1 quindoline-c-MYC G-quadruplex: insights into G-quadruplex-interactive small molecule drug design. *J Am Chem Soc* 133: 17673–17680

Davey SK, Faust EA (1990) Murine DNA polymerase.alpha-primase initiates RNA-primed DNA synthesis preferentially upstream of a 3′-CC(C/A)-5′ motif. *J Biol Chem* 265: 3611–3614

De Cian A, Delemos E, Mergny JL, Teulade-Fichou MP, Monchaud D (2007) Highly efficient G-quadruplex recognition by bisquinolinium compounds. *J Am Chem Soc* 129: 1856–1857

De S, Michor F (2011) DNA secondary structures and epigenetic determinants of cancer genome evolution. *Nat Struct Mol Biol* 18: 950–955

Deegan TD, Baxter J, Ortiz Bazan MA, Yeeles JTP, Labib KPM (2019) Pif1-family helicases support fork convergence during DNA replication termination in eukaryotes. *Mol Cell* 74: 231–244

Di Antonio M, Ponjavic A, Radzevicius A, Ranasinghe RT, Catalano M, Zhang X, Shen J, Needham LM, Lee SF, Klenerman D *et al* (2020) Single-molecule visualization of DNA G-quadruplex formation in live cells. *Nat Chem* 12: 832–837

Douglas ME, Diffley JFX (2021) Budding yeast Rap1, but not telomeric DNA, is inhibitory for multiple stages of DNA replication in vitro. *Nucleic Acids Res* 49: 5671–5683

Edwards DN, Machwe A, Wang Z, Orren DK (2014) Intramolecular telomeric G-quadruplexes dramatically inhibit DNA synthesis by replicative and translesion polymerases, revealing their potential to lead to genetic change. *PloS One* 9: e80664

Fabrini G (2022) UV-Vis_Melting_Analysis. https://githubcom/GiacomoFabrini/UV-Vis_Melting_Analysis/blob/main/UVVis_MeltingCurveAnalysisipynb

Fan JH, Bochkareva E, Bochkarev A, Gray DM (2009) Circular dichroism spectra and electrophoretic mobility shift assays show that human replication protein A binds and melts intramolecular G-quadruplex structures. *Biochemistry* 48: 1099–1111

Fleming AM, Ding Y, Rogers RA, Zhu J, Zhu J, Burton AD, Carlisle CB, Burrows CJ (2017) 4n-1 is a "Sweet Spot" in DNA i-Motif folding of 2′-deoxycytidine homopolymers. *J Am Chem Soc* 139: 4682–4689

Fry M, Loeb LA (1994) The fragile X syndrome d(CGG)n nucleotide repeats form a stable tetrahelical structure. *Proc Natl Acad Sci U S A* 91: 4950–4954

Fry M, Loeb LA (1999) Human werner syndrome DNA helicase unwinds tetrahelical structures of the fragile X syndrome repeat sequence d(CGG)n. *J Biol Chem* 274: 12797–12802

Gacy AM, Goellner G, Juranić N, Macura S, McMurray CT (1995) Trinucleotide repeats that expand in human disease form hairpin structures in vitro. *Cell* 81: 533–540

Gaillard H, Garcia-Muse T, Aguilera A (2015) Replication stress and cancer. *Nat Rev Cancer* 15: 276–289

Gehring K, Leroy JL, Gueron M (1993) A tetrameric DNA structure with protonated cytosine.cytosine base pairs. *Nature* 363: 561–565

Ghosh AK, Rossi ML, Singh DK, Dunn C, Ramamoorthy M, Croteau DL, Liu Y, Bohr VA (2012) RECQL4, the protein mutated in Rothmund-Thomson syndrome, functions in telomere maintenance. *J Biol Chem* 287: 196–209

Grabarczyk DB, Silkenat S, Kisker C (2018) Structural basis for the recruitment of Ctf18-RFC to the replisome. *Structure* 26: 137–144

Guilliam TA, Yeeles JT (2021) The eukaryotic replisome tolerates leading-strand base damage by replicase switching. *EMBO J* 40: e107037

Guo K, Gokhale V, Hurley LH, Sun D (2008) Intramolecularly folded G-quadruplex and i-Motif structures in the proximal promoter of the vascular endothelial growth factor gene. *Nucleic Acids Res* 36: 4598–4608

Hansel-Hertsch R, Beraldi D, Lensing SV, Marsico G, Zyner K, Parry A, Di Antonio M, Pike J, Kimura H, Narita M *et al* (2016) G-quadruplex structures mark human regulatory chromatin. *Nat Genet* 48: 1267–1272

Huber MD, Lee DC, Maizels N (2002) G4 DNA unwinding by BLM and Sgs1p: substrate specificity and substrate-specific inhibition. *Nucleic Acids Res* 30: 3954–3961

Huppert JL, Balasubramanian S (2005) Prevalence of quadruplexes in the human genome. *Nucleic Acids Res* 33: 2908–2916

Huppert JL, Balasubramanian S (2007) G-quadruplexes in promoters throughout the human genome. *Nucleic Acids Res* 35: 406–413

Ivessa AS, Zhou JQ, Schulz VP, Monson EK, Zakian VA (2002) Saccharomyces Rrm3p, a 5′ to 3′ DNA helicase that promotes replication fork progression through telomeric and subtelomeric DNA. *Genes Dev* 16: 1383–1396

Ivessa AS, Lenzmeier BA, Bessler JB, Goudsouzian LK, Schnakenberg SL, Zakian VA (2003) The *Saccharomyces cerevisiae* helicase Rrm3p facilitates replication past nonhistone protein-DNA complexes. *Mol Cell* 12: 1525–1536

Kaiser CE, Van Ert NA, Agrawal P, Chawla R, Yang D, Hurley LH (2017) Insight into the complexity of the i-Motif and G-quadruplex DNA structures formed in the KRAS promoter and subsequent sdrug-induced gene repression. *J Am Chem Soc* 139: 8522–8536

Kendrick S, Kang HJ, Alam MP, Madathil MM, Agrawal P, Gokhale V, Yang D, Hecht SM, Hurley LH (2014) The dynamic character of the BCL2 promoter i-Motif provides a mechanism for modulation of gene expression by compounds that bind selectively to the alternative DNA hairpin structure. *J Am Chem Soc* 136: 4161–4171

Kshirsagar R, Khan K, Joshi MV, Hosur RV, Muniyappa K (2017) Probing the potential role of non-B DNA structures at yeast meiosis-specific DNA double-strand breaks. *Biophys J* 112: 2056–2074

Kumar C, Batra S, Griffith JD, Remus D (2021) The interplay of RNA:DNA hybrid structure and G-quadruplexes determines the outcome of R-loop-replisome collisions. *Elife* 10: e72286

Langston LD, Mayle R, Schauer GD, Yurieva O, Zhang D, Yao NY, Georgescu RE, O'Donnell ME (2017) Mcm10 promotes rapid isomerization of CMG-DNA for replisome bypass of lagging strand DNA blocks. *Elife* 6: e29118

Lee WTC, Yin Y, Morten MJ, Tonzi P, Gwo PP, Odermatt DC, Modesti M, Cantor SB, Gari K, Huang TT *et al* (2021) Single-molecule imaging reveals replication fork coupled formation of G-quadruplex structures hinders local replication stress signaling. *Nat Commun* 12: 2525

Lerner LK, Holzer S, Kilkenny ML, Svikovic S, Murat P, Schiavone D, Eldridge CB, Bittleston A, Maman JD, Branzei D *et al* (2020) Timeless couples G-quadruplex detection with processing by DDX11 helicase during DNA replication. *EMBO J* 39: e104185

Lieblein AL, Furtig B, Schwalbe H (2013) Optimizing the kinetics and thermodynamics of DNA i-Motif folding. *Chembiochem* 14: 1226–1230

Lopes J, Piazza A, Bermejo R, Kriegsman B, Colosio A, Teulade-Fichou MP, Foiani M, Nicolas A (2011) G-quadruplex-induced instability during leading-strand replication. *EMBO J* 30: 4033–4046

Lormand JD, Buncher N, Murphy CT, Kaur P, Lee MY, Burgers P, Wang H, Kunkel TA, Opresko PL (2013) DNA polymerase δ stalls on telomeric lagging strand templates independently from G-quadruplex formation. *Nucleic Acids Res* 41: 10323–10333

MacDougall CA, Byun TS, Van C, Yee MC, Cimprich KA (2007) The structural determinants of checkpoint activation. *Genes Dev* 21: 898–903

Maestroni L, Audry J, Luciano P, Coulon S, Géli V, Corda Y (2020) RPA and Pif1 cooperate to remove G-rich structures at both leading and lagging strand. *Cell Stress* 4: 48–63

Maiti S (2010) Human telomeric G-quadruplex. *FEBS J* 277: 1097

Malliavin TE, Gau J, Snoussi K, Leroy JL (2003) Stability of the i-Motif structure is related to the interactions between phosphodiester backbones. *Biophys J* 84: 3838–3847

Martella M, Pichiorri F, Chikhale RV, Abdelhamid MAS, Waller ZAE, Smith SS (2022) i-Motif formation and spontaneous deletions in human cells. *Nucleic Acids Res* 50: 3445–3455

Mergny JL, Lacroix L (2003) Analysis of thermal melting curves. *Oligonucleotides* 13: 515–537

Mergny JL, Li J, Lacroix L, Amrane S, Chaires JB (2005) Thermal difference spectra: a specific signature for nucleic acid structures. *Nucleic Acids Res* 33: e138

Miglietta G, Cogoi S, Pedersen EB, Xodo LE (2015) GC-elements controlling HRAS transcription form i-Motif structures unfolded by heterogeneous ribonucleoprotein particle A1. *Sci Rep* 5: 18097

Mirkin SM, Lyamichev VI, Drushlyak KN, Dobrynin VN, Filippov SA, Frank-Kamenetskii MD (1987) DNA H form requires a homopurine-homopyrimidine mirror repeat. *Nature* 330: 495–497

Murat P, Guilbaud G, Sale JE (2020) DNA polymerase stalling at structured DNA constrains the expansion of short tandem repeats. *Genome Biol* 21: 209

Nadel Y, Weisman-Shomer P, Fry M (1995) The fragile X syndrome single strand d(CGG)n nucleotide repeats readily fold back to form unimolecular hairpin structures. *J Biol Chem* 270: 28970–28977

Ou TM, Lu YJ, Tan JH, Huang ZS, Wong KY, Gu LQ (2008) G-quadruplexes: targets in anticancer drug design. *ChemMedChem* 3: 690–713

Paeschke K, Capra JA, Zakian VA (2011) DNA replication through G-quadruplex motifs is promoted by the Saccharomyces cerevisiae Pif1 DNA helicase. *Cell* 145: 678–691

Paeschke K, Bochman ML, Garcia PD, Cejka P, Friedman KL, Kowalczykowski SC, Zakian VA (2013) Pif1 family helicases suppress genome instability at G-quadruplex motifs. *Nature* 497: 458–462

Papadopoulou C, Guilbaud G, Schiavone D, Sale JE (2015) Nucleotide pool depletion induces G-quadruplex-dependent perturbation of gene expression. *Cell Rep* 13: 2491–2503

Piazza A, Adrian M, Samazan F, Heddi B, Hamon F, Serero A, Lopes J, Teulade-Fichou MP, Phan AT, Nicolas A (2015) Short loop length and high thermal stability determine genomic instability induced by G-quadruplex-forming minisatellites. *EMBO J* 34: 1718–1734

Plesa C, Verschueren D, Pud S, van der Torre J, Ruitenberg JW, Witteveen MJ, Jonsson MP, Grosberg AY, Rabin Y, Dekker C (2016) Direct observation of DNA knots using a solid-state nanopore. *Nat Nanotechnol* 11: 1093–1097

Ray S, Qureshi MH, Malcolm DW, Budhathoki JB, Celik U, Balci H (2013) RPA-mediated unfolding of systematically varying G-quadruplex structures. *Biophys J* 104: 2235–2245

Ribeyre C, Lopes J, Boule JB, Piazza A, Guedin A, Zakian VA, Mergny JL, Nicolas A (2009) The yeast Pif1 helicase prevents genomic instability caused by G-quadruplex-forming CEB1 sequences in vivo. *PLoS Genet* 5: e1000475

Robinson J, Raguseo F, Nuccio SP, Liano D, Di Antonio M (2021) DNA G-quadruplex structures: more than simple roadblocks to transcription? *Nucleic Acids Res* 49: 8419–8431

Rogers CM, Wang JC, Noguchi H, Imasaki T, Takagi Y, Bochman ML (2017) Yeast Hrq1 shares structural and functional homology with the disease-linked human RecQ4 helicase. *Nucleic Acids Res* 45: 5217–5230

Salas TR, Petruseva I, Lavrik O, Bourdoncle A, Mergny JL, Favre A, Saintomé C (2006) Human replication protein A unfolds telomeric G-quadruplexes. *Nucleic Acids Res* 34: 4857–4865

Samora CP, Saksouk J, Goswami P, Wade BO, Singleton MR, Bates PA, Lengronne A, Costa A, Uhlmann F (2016) Ctf4 links DNA replication with sister chromatid cohesion establishment by recruiting the Chl1 helicase to the replisome. *Mol Cell* 63: 371–384

Sarkies P, Reams C, Simpson LJ, Sale JE (2010) Epigenetic instability due to defective replication of structured DNA. *Mol Cell* 40: 703–713

van Schendel R, Romeijn R, Buijs H, Tijsterman M (2021) Preservation of lagging strand integrity at sites of stalled replication by Pol alpha-primase and 9-1-1 complex. *Sci Adv* 7: eabf2278

Schiavone D, Guilbaud G, Murat P, Papadopoulou C, Sarkies P, Prioleau MN, Balasubramanian S, Sale JE (2014) Determinants of G quadruplex-induced epigenetic instability in REV1-deficient cells. *EMBO J* 33: 2507–2520

Scior A, Preissler S, Koch M, Deuerling E (2011) Directed PCR-free engineering of highly repetitive DNA sequences. *BMC Biotechnol* 11: 87

Sen D, Gilbert W (1988) Formation of parallel four-stranded complexes by guanine-rich motifs in DNA and its implications for meiosis. *Nature* 334: 364–366

Shastri N, Tsai YC, Hile S, Jordan D, Powell B, Chen J, Maloney D, Dose M, Lo Y, Anastassiadis T *et al* (2018) Genome-wide identification of structure-forming repeats as principal sites of fork collapse upon ATR inhibition. *Mol Cell* 72: 222–238

Simonsson T, Pribylova M, Vorlickova M (2000) A nuclease hypersensitive element in the human c-myc promoter adopts several distinct i-tetraplex structures. *Biochem Biophys Res Commun* 278: 158–166

Sparks JL, Chistol G, Gao AO, Raschle M, Larsen NB, Mann M, Duxin JP, Walter JC (2019a) The CMG helicase bypasses DNA-protein cross-links to facilitate their repair. *Cell* 176: 167–181

Sparks MA, Singh SP, Burgers PM, Galletto R (2019b) Complementary roles of Pif1 helicase and single stranded DNA binding proteins in stimulating DNA replication through G-quadruplexes. *Nucleic Acids Res* 47: 8595–8605

Stokes K, Winczura A, Song B, Piccoli G, Grabarczyk DB (2020) Ctf18-RFC and DNA Pol form a stable leading strand polymerase/clamp loader complex required for normal and perturbed DNA replication. *Nucleic Acids Res* 48: 8128–8145

Sun H, Karow JK, Hickson ID, Maizels N (1998) The Bloom's syndrome helicase unwinds G4 DNA. *J Biol Chem* 273: 27587–27592

Takahashi S, Brazier JA, Sugimoto N (2017) Topological impact of noncanonical DNA structures on Klenow fragment of DNA polymerase. *Proc Natl Acad Sci U S A* 114: 9605–9610

Taylor MRG, Yeeles JTP (2018) The initial response of a eukaryotic replisome to DNA damage. *Mol Cell* 70: e1012

Thys RG, Wang YH (2015) DNA replication dynamics of the GGGGCC repeat of the C9orf72 gene. *J Biol Chem* 290: 28953–28962

Tubbs A, Sridharan S, van Wietmarschen N, Maman Y, Callen E, Stanlie A, Wu W, Wu X, Day A, Wong N *et al* (2018) Dual roles of poly(dA:dT) tracts in replication initiation and fork collapse. *Cell* 174: 1127–1142

Vannier JB, Sandhu S, Petalcorin MI, Wu X, Nabi Z, Ding H, Boulton SJ (2013) RTEL1 is a replisome-associated helicase that promotes telomere and genome-wide replication. *Science* 342: 239–242

Voineagu I, Narayanan V, Lobachev KS, Mirkin SM (2008) Replication stalling at unstable inverted repeats: interplay between DNA hairpins and fork stabilizing proteins. *Proc Natl Acad Sci U S A* 105: 9936–9941

Wang G, Vasquez KM (2017) Effects of replication and transcription on DNA structure-related genetic instability. *Genes (Basel)* 8: 17

van Wietmarschen N, Merzouk S, Halsema N, Spierings DCJ, Guryev V, Lansdorp PM (2018) BLM helicase suppresses recombination at G-quadruplex motifs in transcribed genes. *Nat Commun* 9: 271

Wright EP, Huppert JL, Waller ZAE (2017) Identification of multiple genomic DNA sequences which form i-Motif structures at neutral pH. *Nucleic Acids Res* 45: 2951–2959

Wu Y, Shin-ya K, Brosh RM Jr (2008) FANCJ helicase defective in Fanconia anemia and breast cancer unwinds G-quadruplex DNA to defend genomic stability. *Mol Cell Biol* 28: 4116–4128

Wu Y, Sommers JA, Khan I, de Winter JP, Brosh RM Jr (2012) Biochemical characterization of Warsaw breakage syndrome helicase. *J Biol Chem* 287: 1007–1021

Yeeles JT, Deegan TD, Janska A, Early A, Diffley JF (2015) Regulated eukaryotic DNA replication origin firing with purified proteins. *Nature* 519: 431–435

Yeeles JTP, Janska A, Early A, Diffley JFX (2017) How the eukaryotic replisome achieves rapid and efficient DNA replication. *Mol Cell* 65: 105–116

Yu CE, Oshima J, Fu YH, Wijsman EM, Hisama F, Alisch R, Matthews S, Nakura J, Miki T, Ouais S *et al* (1996) Positional cloning of the Werner's syndrome gene. *Science* 272: 258–262

Yuan Z, Georgescu R, Schauer GD, O'Donnell ME, Li H (2020) Structure of the polymerase epsilon holoenzyme and atomic model of the leading strand replisome. *Nat Commun* 11: 3156

Zeman MK, Cimprich KA (2014) Causes and consequences of replication stress. *Nat Cell Biol* 16: 2–9

Zeraati M, Langley DB, Schofield P, Moye AL, Rouet R, Hughes WE, Bryan TM, Dinger ME, Christ D (2018) I-Motif DNA structures are formed in the nuclei of human cells. *Nat Chem* 10: 631–637

Zhou JC, Janska A, Goswami P, Renault L, Abid Ali F, Kotecha A, Diffley JFX, Costa A (2017) CMG-Pol epsilon dynamics suggests a mechanism for the establishment of leading-strand synthesis in the eukaryotic replisome. *Proc Natl Acad Sci U S A* 114: 4141–4146

Expanded View Figures

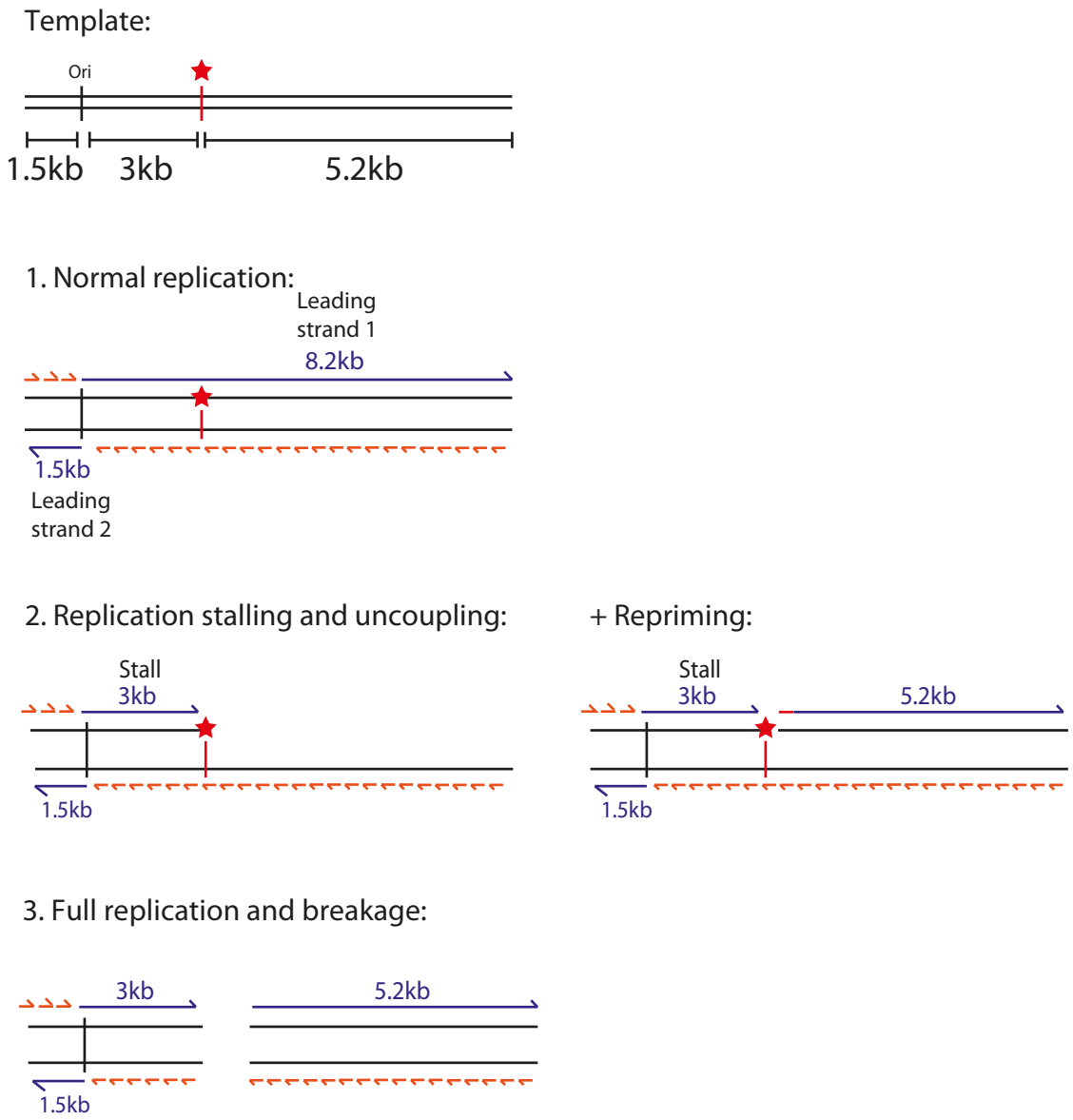

Figure EV1. Schematic of potential replication products from G4 and iM-containing templates.

Position of the origin of replication is marked as 'ori' from which replication initiates through sequence-specific replisome loading. Two forks initiate from the origin and generate one longer rightward moving fork of 8.2 kb ('Leading strand 1') and one shorter leftward moving fork of 1.5 kb ('Leading strand 2'). Lagging strand products are synthesised as short Okazaki fragments. The multiple cloning site (indicated by a red star) is positioned 3 kb downstream of the origin and was used to insert various G4 or iM-forming sequences into the template. This means that only the rightward moving fork would encounter them and therefore 'leading strand 2' can serve as an internal control. Under conditions of replication stalling, helicase-polymerase uncoupling may occur which may be associated with intrinsic repriming at the site of fork stalling. Replication products may also break at the site of the insert during or after replication.

Figure EV2. Quantification of replisome stalling at G4s and iMs in relation to their biophysical characteristics.

A Quantification of stall intensities from three independent experiments of substrates, as shown in Fig 1B. The 3 kb stalling intensity band was normalised to the intensity of 'leading strand 2' in each lane to account for variation in the efficiencies of reactions for each substrate. The mean stalling intensity is plotted with error bars representing the standard error.

B Melting temperatures of the G4s formed by sequences tested in Fig 1B versus their stalling intensities as calculated in (A). Line indicates simple linear regression with a Pearson correlation *r* value of 0.76.

C Quantification of stall intensities as in (A) from three independent experiments of substrates as shown in Fig 1C.

D Melting temperatures of the iMs formed by sequences tested in Fig 1C versus their stalling intensities as calculated in Fig EV2C. Line indicates simple linear regression with Pearson correlation *r* value of −0.34.

E The transitional pH (pH_T) of the iMs formed by the sequences tested in Fig 1C versus their stalling intensities as presented in calculated in Fig EV2C. Line indicates simple linear regression with a Pearson correlation *r* value of 0.27.

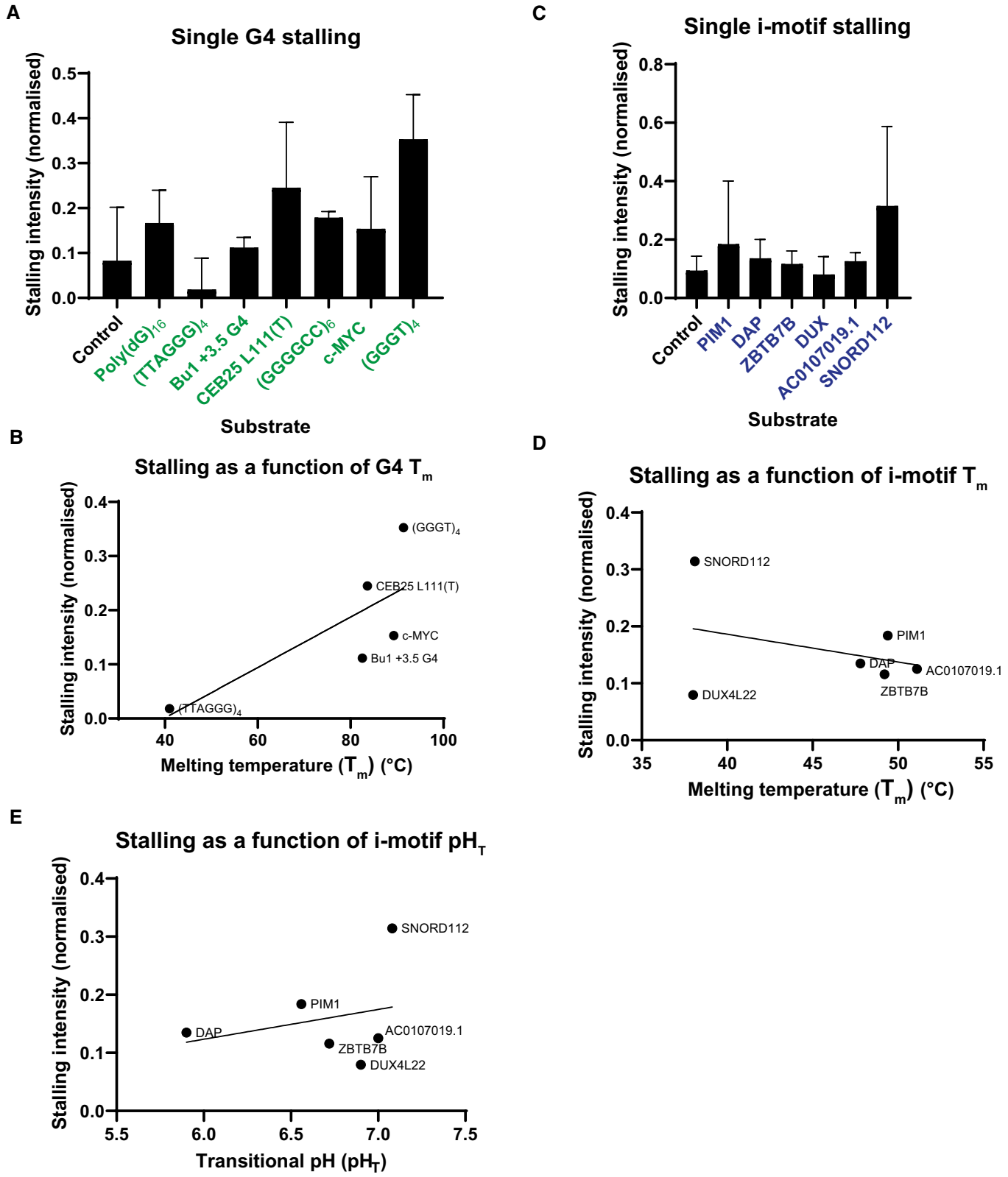

Figure EV2.

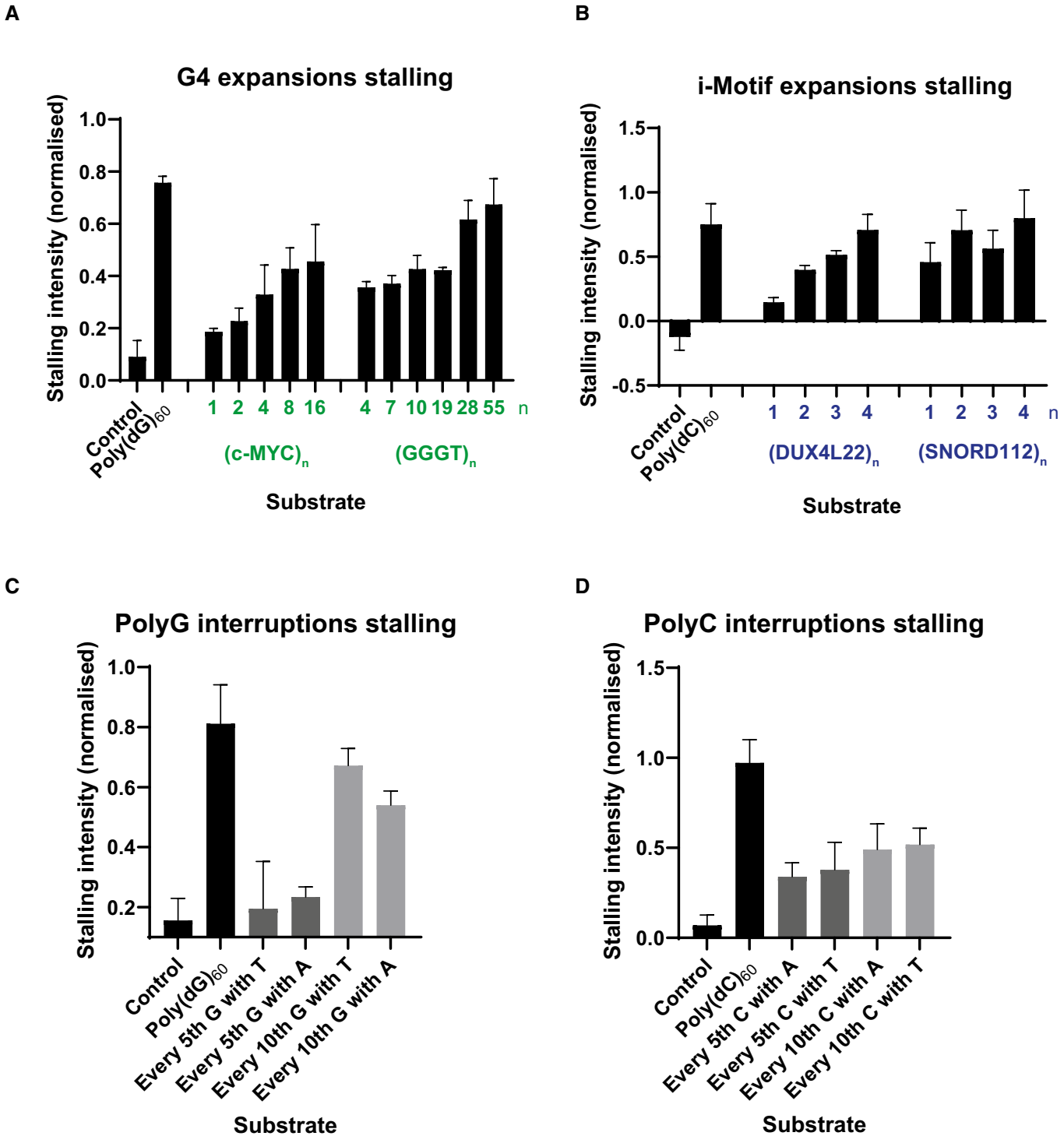

Figure EV3. The effect of increased consecutive quadruplex sequences and interrupting tracts of poly(dC)$_{60}$ or poly(dC)$_{60}$ on replisome stalling.

A–D Quantification of stall intensities from three independent experiments of relevant substrates, as indicated in Fig 2A–D. The 3 kb stalling intensity band was normalised to the intensity of 'leading strand 2' in each lane to account for variation in the efficiencies of reactions for each substrate. The mean stalling intensity is plotted with error bars representing the standard error.

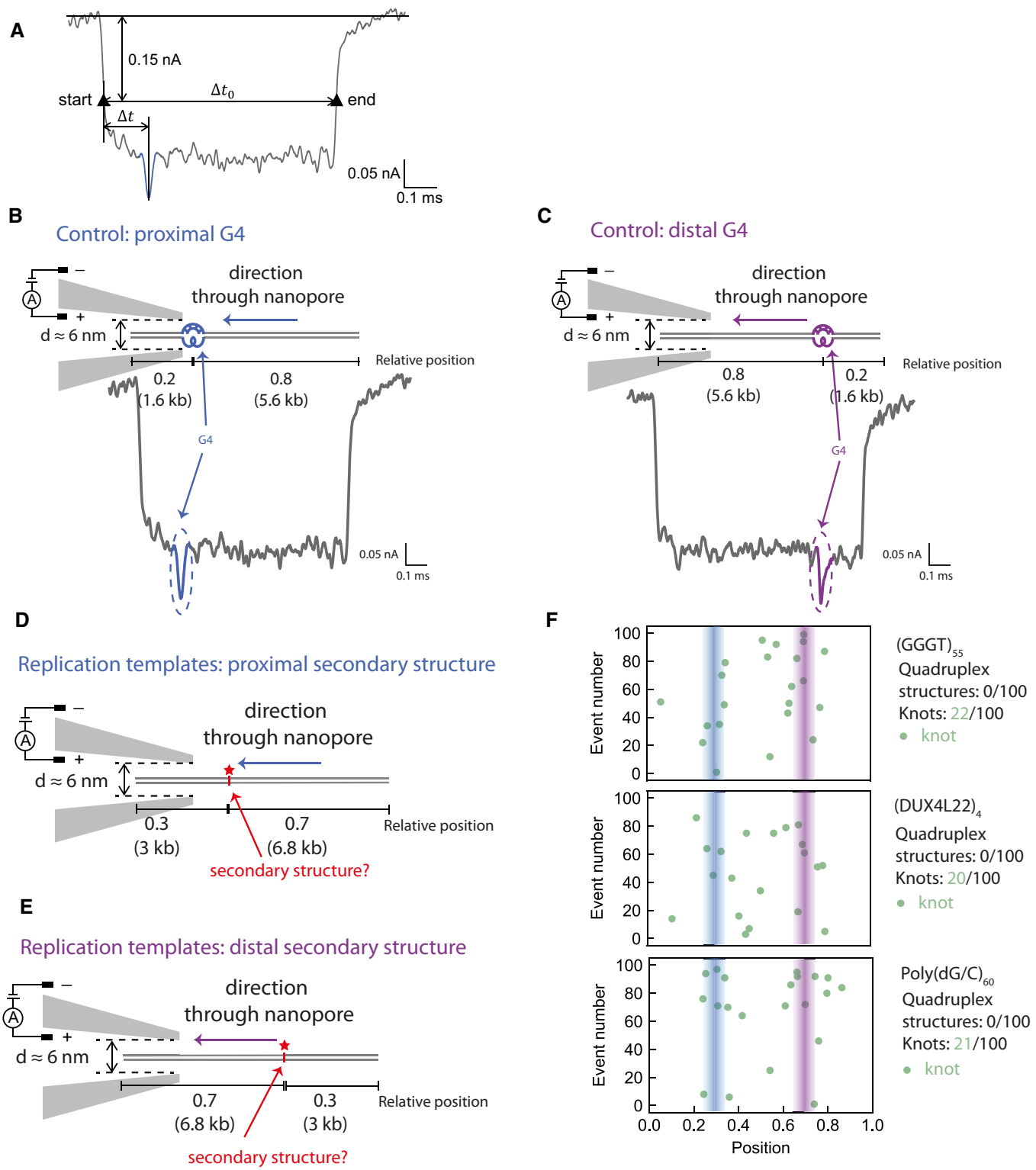

Figure EV4.

Figure EV4. Single molecule nanopore experiments to detect secondary structures.

A A representative event of our nanopore measurements. The two black triangles, namely the two intersections of the reference line 0.15 nA below the current baseline and the event current trace, mark the start and end of one event. Δt_0 refers to the timescale between the start and end, and Δt refers to the interval between second-level peak and the start.

B, C Schematic of a positive control DNA passing through the nanopore in the direction that positions the G4 proximally (B) or distally (C), and a representative nanopore measurement event. Numbers indicate the proportion through the template the G4 is positioned. The G-quadruplex structure and its corresponding current drop are marked in blue (B) or purple (C).

D, E Schematic of DNA replication templates passing through the nanopore in the direction that positions the potential secondary structures proximally (D) or distally (E). Numbers indicate the proportion through the template the secondary structure-forming sequence is positioned.

F Nanopore measurement results of $(GGGT)_{55}$, $(DUX4L22)_4$ and Poly$(dG/C)_{60}$. Lines indcate expected positions of secondary structures.

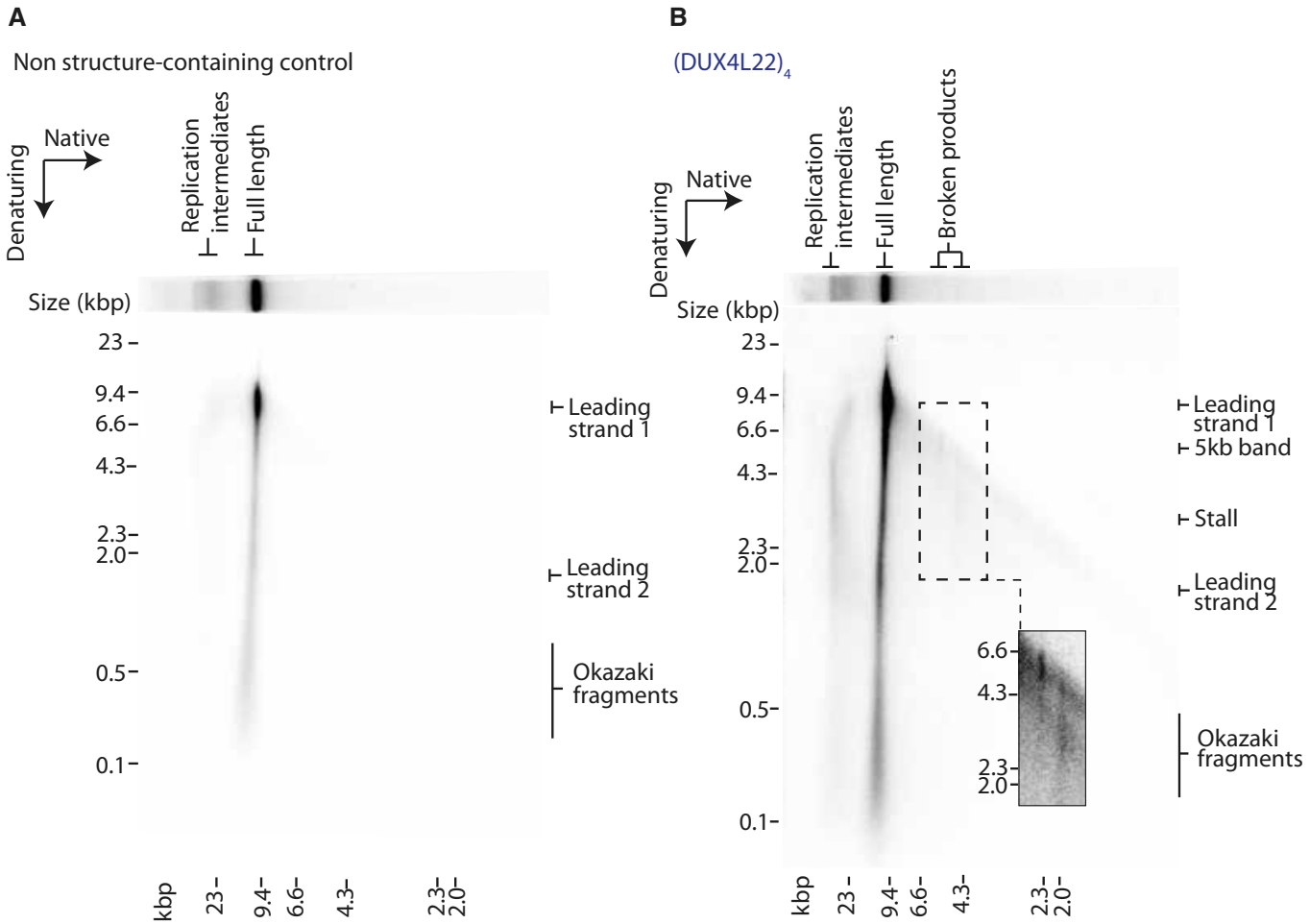

Figure EV5. Analysis of replication products by two-dimensional (2D) gel electrophoresis.

A, B Analysis of replication products of control (A) or iM (B) substrates by 2D gels. Replicated products were run firstly in the native dimension and subsequently in the denaturing dimension.

TABLE OF CONTENTS

Appendix Figure S1

A

G4 mutated substrates	Sequence (5' - 3')
c-MYC	TGA**GGG**TGG**GG**TA**GGG**TGG**GG**TAA
c-MYC MUT	TGAGAGTGAGTAGAGTGAGTAA
$(GGGT)_4$	**GGG**TGG**GG**TGG**GG**T
$(GGGT)_3$	**GGG**TGG**GG**TGG**GG**T
CEB25 L111(T) (Piazza et al., 2015)	AA**GGG**TGG**GG**TGG**GG**TGG**GG**TGTGAGT GT**GGG**TGTGGAGGTAGATGT
CEB25 L111(A) (Piazza et al., 2015)	AA**GGG**A**GGG**A**GGG**A**GGG**TGTGAG TGT**GGG**TGTGGAGGTAGATGT

B

iMotif mutated substrates	Sequence (5'-3')
DUX4L22	**CCCCC**GAAACGCG**CCCCCC**T**CCCCCC**T**C CCCCC**TCT**CCCCC**
DUX4L22 MUT	CCTCCGAAACGCGCCTTCCTCCTTCCT CCTTCCTCTCCTCC
SNORD112	**CCCCCCCCC**G**CCCCCC**A**CCCCCCC**A**CCCC CCCCCCC**
SNORD112 MUT	CCTCCTTCCGCCTTCCACCTTCTCACC TCCTCCTCC

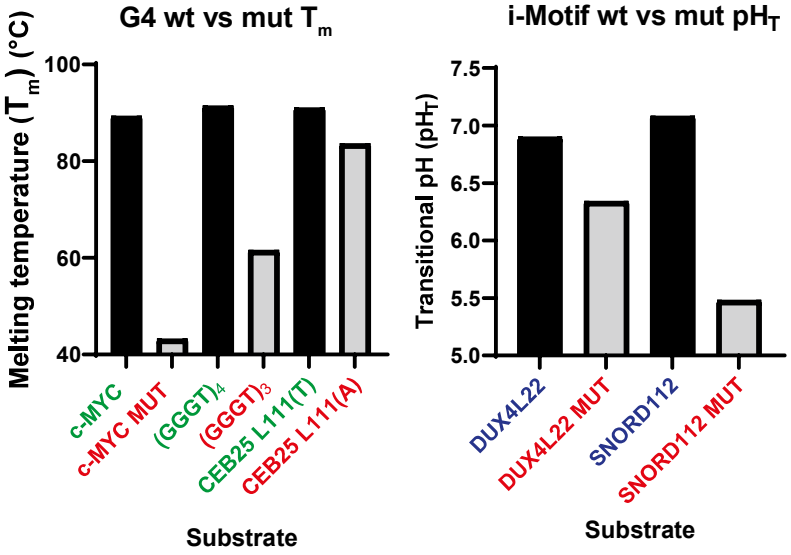

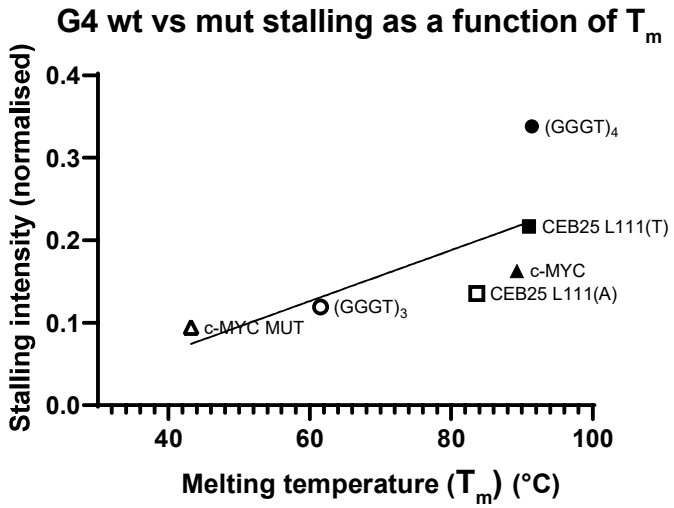

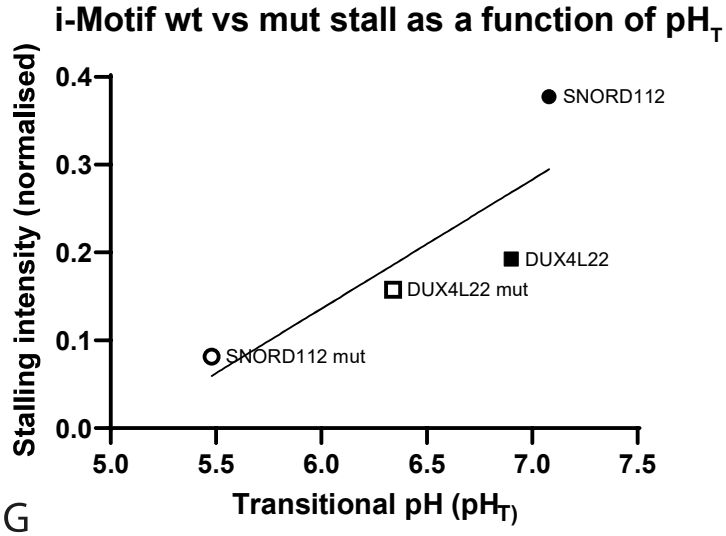

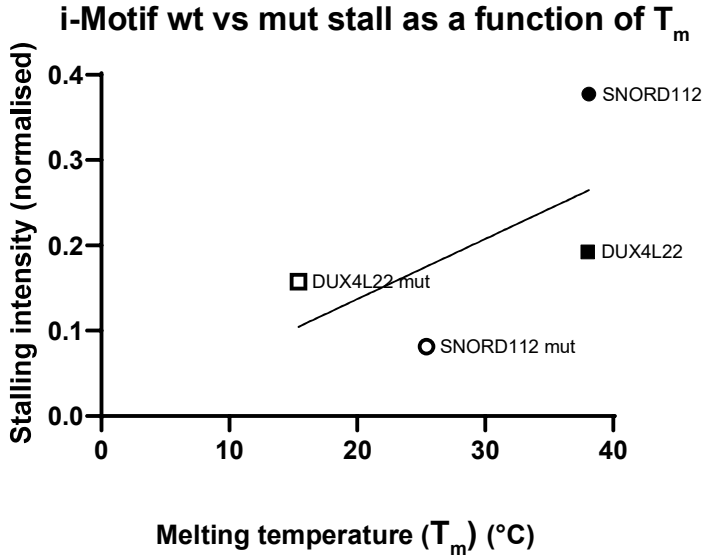

Appendix Figure S1. Correlations between biophysical properties of mutated G4 and iMs and replisome stalling. (A and B) Sequences of wildtype or mutated G4 (A) or iM-forming (B) sequences used to generate substrates for replication reactions in Fig. 1D and 1F. Mutated sequences (depicted in red) have abrogated or weakened ability to form structures. (C) Melting temperatures of the secondary structures formed by sequences depicted in Fig. 1D. (D) The transitional pH (pHT) of the structures formed by the sequences depicted in Fig. 1F. (E) Melting temperatures of the structures formed by sequences tested in Fig. 1D versus their stalling intensities as calculated in Fig. 1E. Line indicates simple linear regression with Pearson correlation r value of 0.7. (F and G) Transitional pH (pH_T) (F) or melting temperature (G) of the structures formed by sequences tested in Fig. 1F versus their stalling intensities as calculated in Fig. 1G. Lines indicate simple linear regression with Pearson correlation r values of 0.8 (F) and 0.6 (G).

Appendix Figure S2

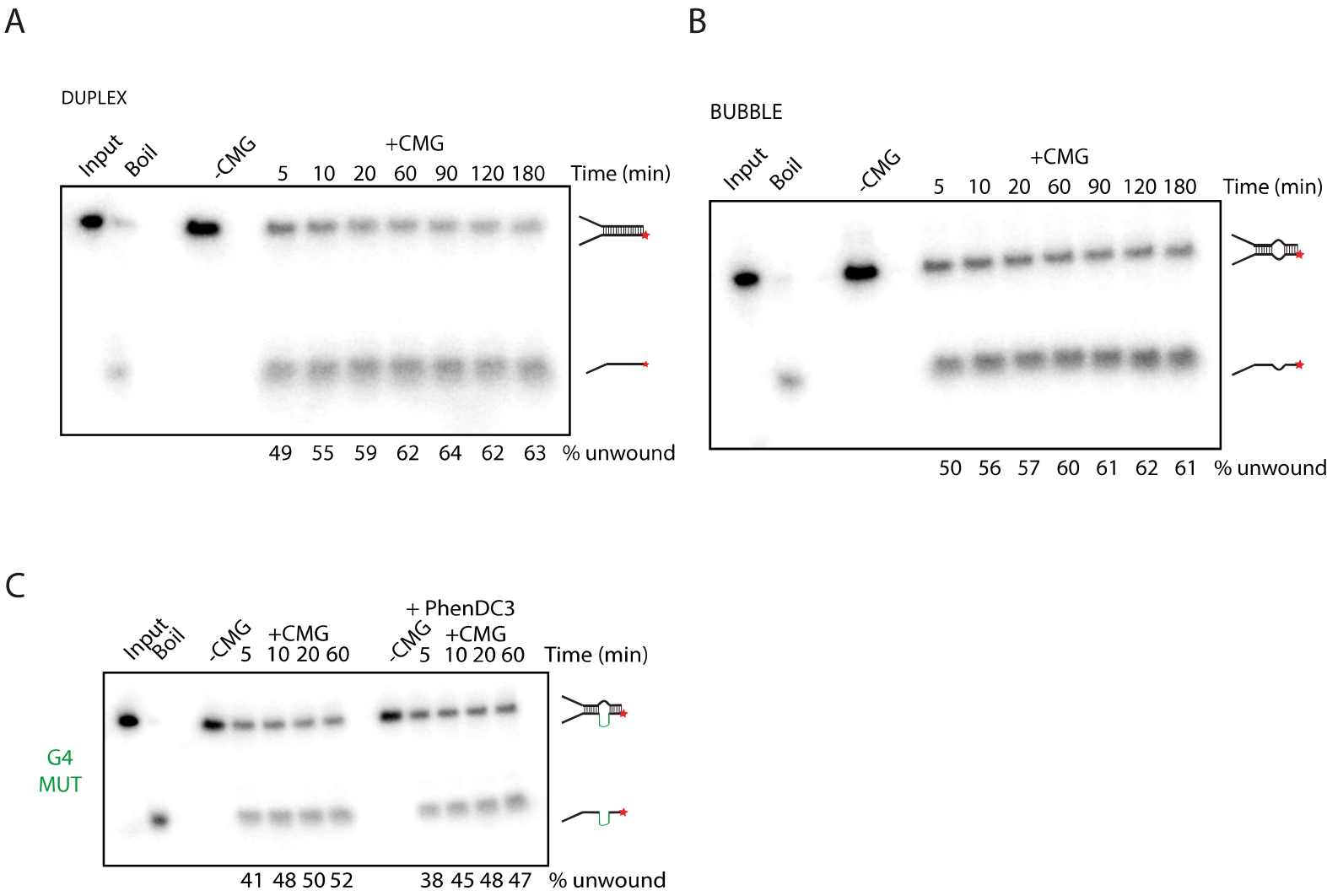

Appendix Figure S2. Unwinding of non-structure containing substrates by CMG.
(A-B) CMG unwinding assays on substrates containing duplex (A) or a poly(dT)$_{19}$ bubble (B). CMG unwinding was stimulated by the addition of 2 nM ATP following CMG loading in the presence of ATPγS. Samples were taken at the indicated time points. Products were run on 10% TBE gels. Input and boiled substrates were used as controls to visualise where original and unwound substrates run on the gel. The proportion of template unwound was calculated by measuring the intensity of the 'unwound' product band as a proportion of the total product intensity for each lane. (C) CMG unwinding assays on substrates containing G4 mutant sequence. Reactions were carried out as in (B) but with the addition of 0.25 μM PhenDC3 where indicated.

Appendix Figure S3

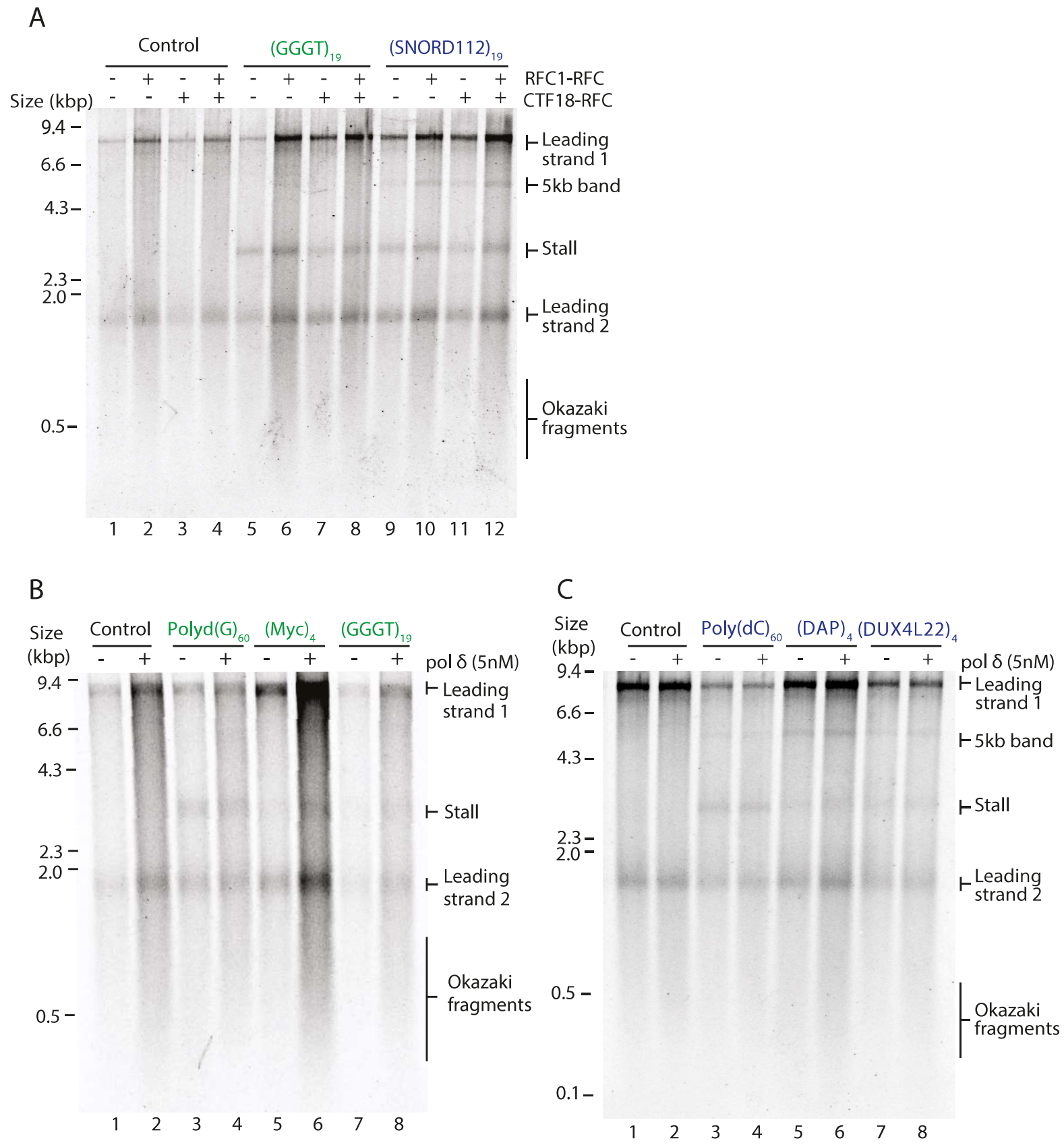

Appendix Figure S3. Pol δ and CTF18-RFC do not affect replisome stalling at G4s or iMs.
(A) Replication of substrates containing a G4 ($(GGGT)_{19}$) or iM ($(SNORD112)_1$) in the presence or absence of RFC1-RFC or CTF18-RFC as indicated. Products were visualised on a denaturing agarose gel.
(B and C) Analysis of replication products of G4 (B) or iM (C) substrates in the presence or absence of pol δ on denaturing agarose gels.

Appendix Figure S4

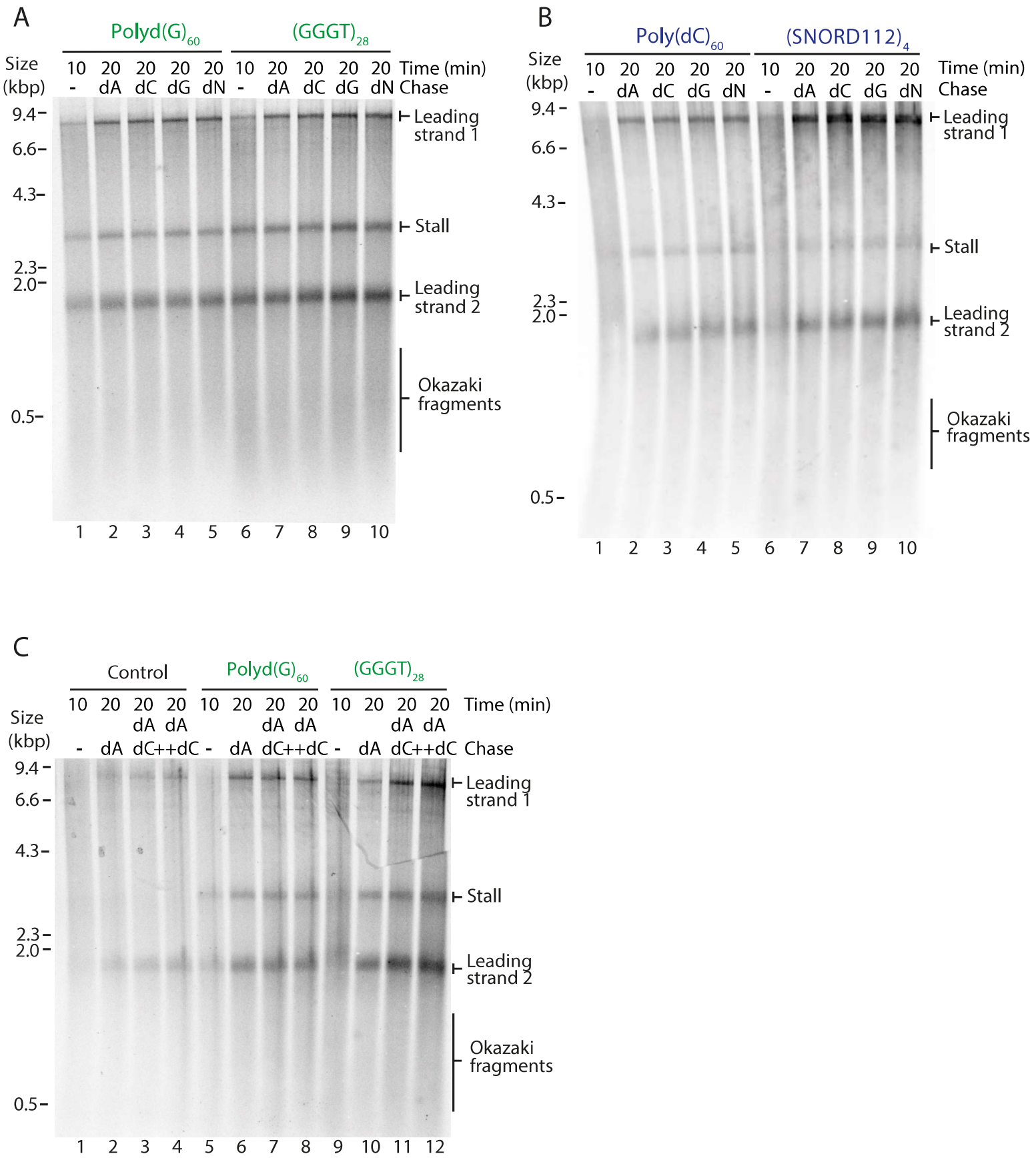

Appendix Figure S4. Excess dNTPs can not rescue stalling at G4s or iMs.
(A and B) Pulse-chase experiments carried out with the indicated templates.
Reactions were initiated with radiolabelled dATP for 10 min and chased for another 10 min with either excess 'cold' dATP alone (dA) or in combination with dCTP (dC), dGTP (dG), or all four dNTPs (dN). (C) As per A and B but reactions were chased with either 'cold' dATP alone or in combination with the same excess of dCTP or with double the excess of dCTP as dATP.

Appendix Figure S5

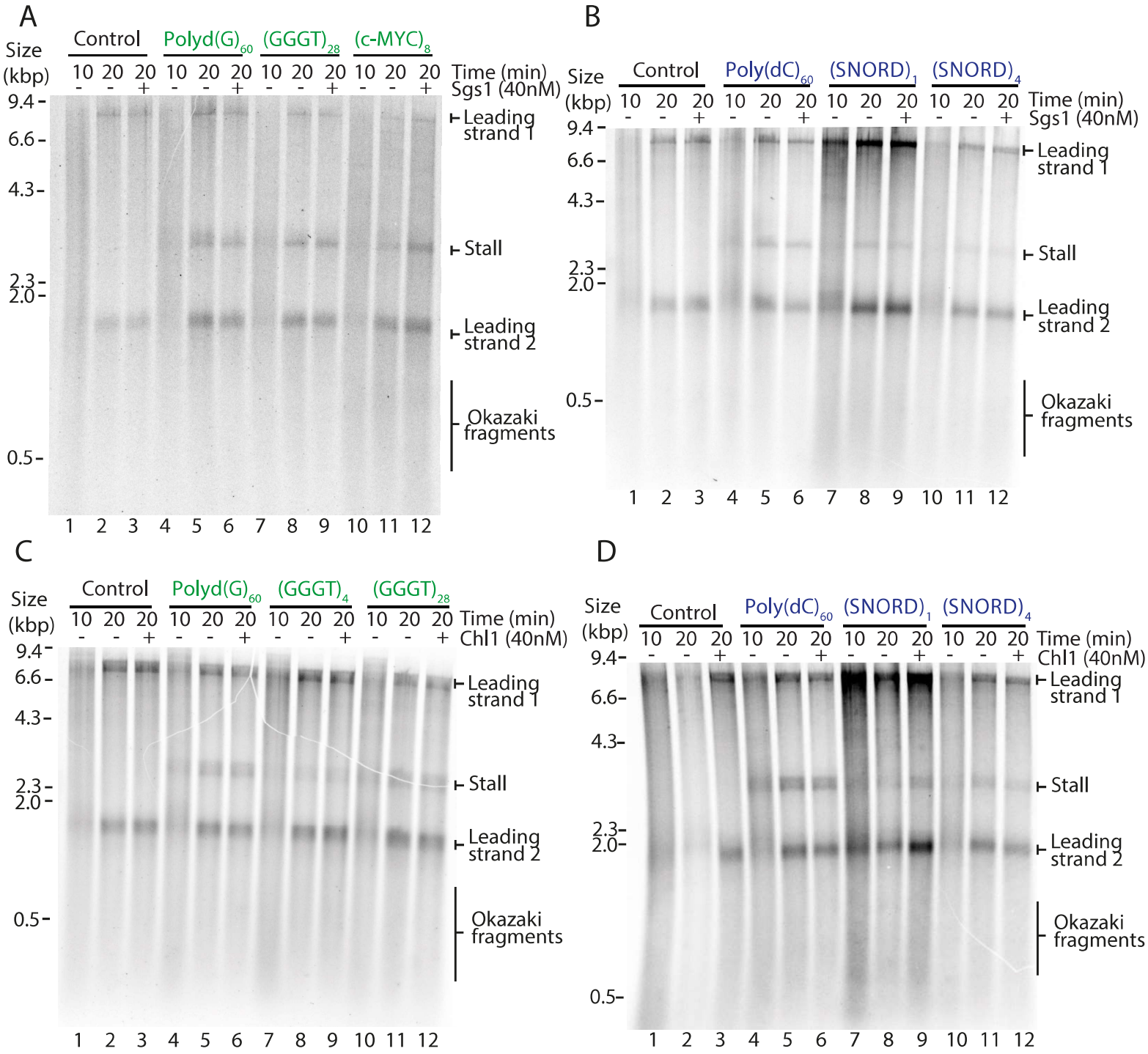

Appendix Figure S5. Sgs1, Chl1, Rrm3 and Hrq1 are unable to rescue replication stalling at G4s or iMs. (A-F) Pulse-chase experiments carried out with the indicated templates. Reactions were initiated with radiolabelled dATP. After a 10 min pulse, either Sgs1 (A and B), Chl1 (C and D), Rrm3 (E) or Hrq1 (F) (wildtype or an ATPase dead mutant, K318A) was added with the chase and samples taken after another 10 min. (G-J) Helicase unwinding assays using purified Sgs1 (G), Chl1 (H), Rrm3 (I) or Hrq1 (wildtype or K318A mutant) (J) . Time points were taken as indicated. Products were run on 10% TBE gels. Input and boiled substrates were used as controls to visualise where original and unwound substrates run on the gel. Assays demonstrate that both Sgs1 and Chl1 show robust unwinding activity, Rrm3 and Hrq1 show partial activity.

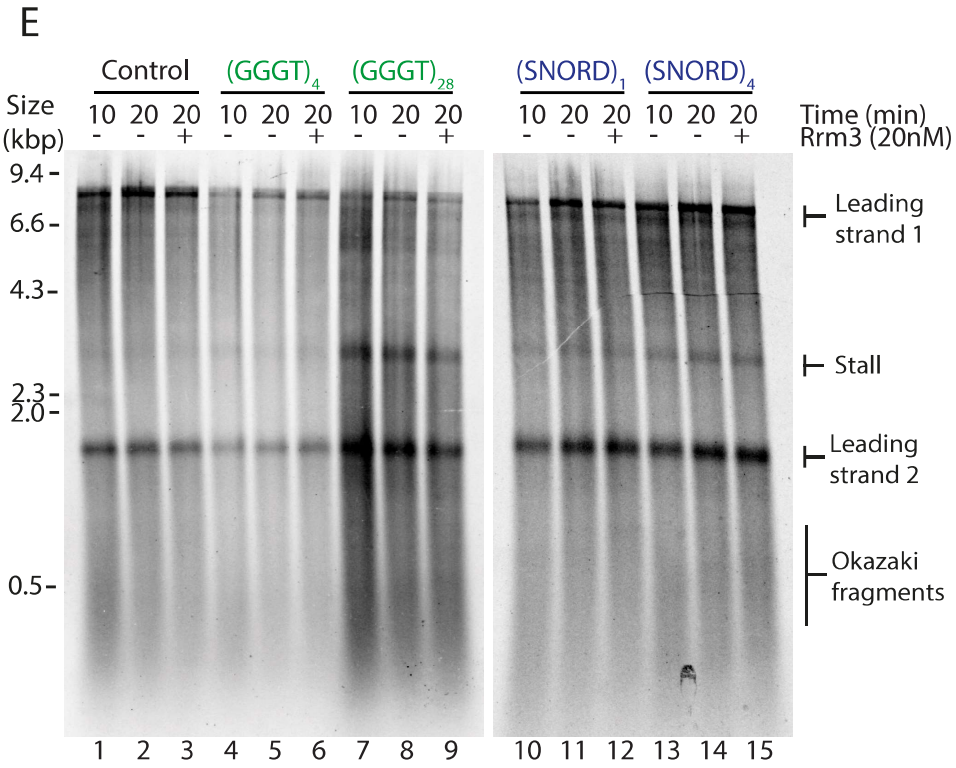
E
Control
(GGGT)4
(GGGT)28
(SNORD)1
(SNORD)4
Size (kbp)
10 20 20 10 20 20 10 20 20 10 20 20 10 20 20
- - + - - + - - + - - + - - +
Time (min)
Rrm3 (20nM)
9.4
6.6
4.3
2.3
2.0
0.5
Leading strand 1
Stall
Leading strand 2
Okazaki fragments
1 2 3 4 5 6 7 8 9 10 11 12 13 14 15

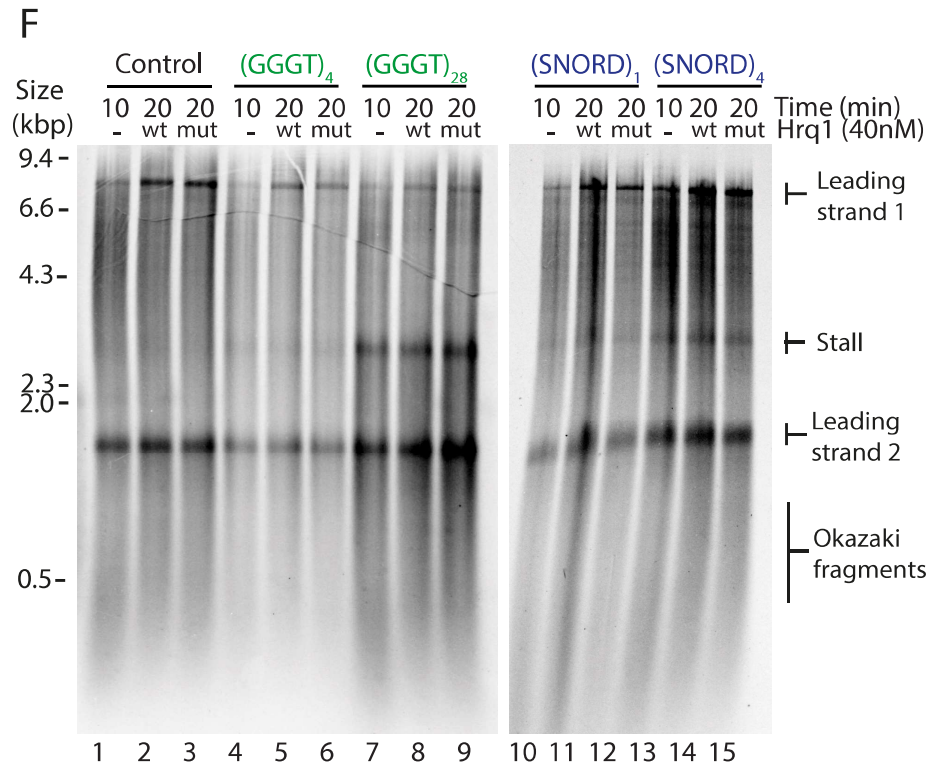
F
Control
(GGGT)4
(GGGT)28
(SNORD)1
(SNORD)4
Size (kbp)
10 20 20 10 20 20 10 20 20 10 20 20 10 20 20
- wt mut - wt mut - wt mut - wt mut - wt mut
Time (min)
Hrq1 (40nM)
9.4
6.6
4.3
2.3
2.0
0.5
Leading strand 1
Stall
Leading strand 2
Okazaki fragments
1 2 3 4 5 6 7 8 9 10 11 12 13 14 15

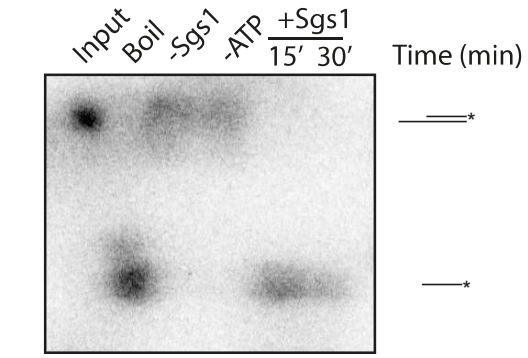
G
Input
Boil
-Sgs1
-ATP
+Sgs1
15′ 30′
Time (min)

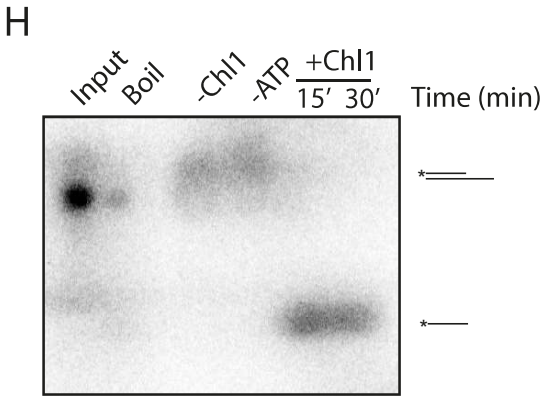
H
Input
Boil
-Chl1
-ATP
+Chl1
15′ 30′
Time (min)

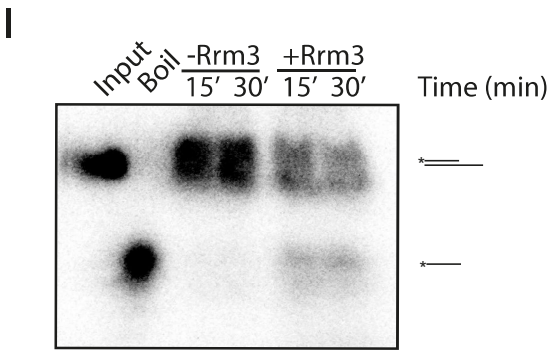
I
Input
Boil
-Rrm3
15′ 30′
+Rrm3
15′ 30′
Time (min)

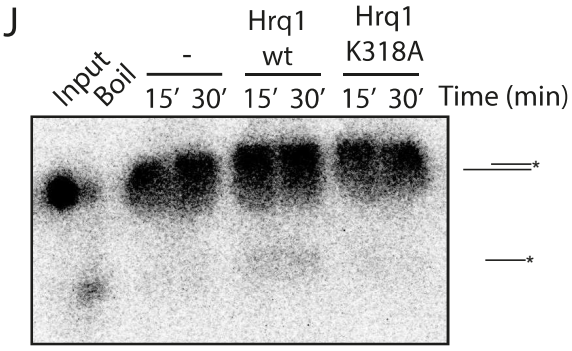
J
Input
Boil
-
15′ 30′
Hrq1 wt
15′ 30′
Hrq1 K318A
15′ 30′
Time (min)